CrossMark

ORIGINAL PAPER

"Normal" to adakite-like arc magmatism associated with the El Abra porphyry copper deposit, Central Andes, Northern Chile

Osvaldo M. Rabbia[1] · Karen J. Correa[2] · Laura B. Hernández[1] · Thomas Ulrich[3]

Abstract The El Abra porphyry copper deposit belongs to the Late Eocene—Early Oligocene metallogenic belt of northern Chile, which host several world-class porphyry copper deposits. Our previous geochronological work done on this deposit provides the temporal framework for petrological data interpretation. The magmatic history of the El Abra deposit lasts for ~8.6 Ma and can be divided into two stages. An early period, from about 45 to ~38.7 Ma, dominated by diorites and quartz monzodiorites with "normal" (non-adakite) arc geochemistry and a late period, with rocks younger than ~38.7 Ma that developed adakite-like geochemistry, where equigranular granodiorites are the volumetrically dominant rock type (e.g., Clara granodiorite~38 Ma). These granodiorites are then intruded by leucocratic porphyry dikes and aplites. Most copper mineralization is associated with multiple intrusions of these younger porphyritic rocks, described as the El Abra porphyry unit, and emplaced over a ~1.4 Ma period, from ~37.5 to 36.1 Ma. The adakite-like geochemistry of the younger rock units (<38.7 Ma) is attested by a significant depletion in REE contents, particularly MREE and HREE (concave MREE distribution patterns), high La/Yb and Sr/Y ratios, and Na_2O and Al_2O_3 contents, along with the absence of the Eu anomaly in normalized REE distribution patterns. The evolution of this large, long-lived magmatic system from "normal" to adakite-like arc magmatism is discussed in a tectonic context of crust overthickening due to a major orogenic episode (Incaic compressive phase). This tectonic setting may have promoted higher pressure conditions at the lower crust "hot zone" and increased the crustal residence time of derivative melts favoring extensive differentiation leading to water-rich (and oxidized?) felsic melts, where amphibole fractionation played an important role. Strontium, Nd, and Pb isotope data suggest a common mantle source for both the non-adakite and adakite-like rocks. This implies that these two groups of rocks from the El Abra porphyry copper deposit may have largely resulted from the different crustal conditions under which they have evolved.

Keywords Adakite-like rocks · Amphibole-rich rocks · Porphyry copper · El Abra · Central Andes

✉ Osvaldo M. Rabbia
rabbia@udec.cl

1   Instituto de Geología Económica Aplicada, Universidad de Concepción, Casilla 160 C, Concepción, Chile

2   Departamento de Ciencias de la Tierra, Universidad de Concepción, Casilla 160 C, Concepción, Chile

3   Institute for Geoscience, Aarhus University, Hoegh-Guldbergs Gade 2, 8000 Aarhus, Denmark

Introduction

Most porphyry copper deposits are genetically related to calc-alkaline magmatic arcs developed above active subduction zones at converging plate margins (e.g., Sillitoe 1972; Richards 2003, 2009). A classic example of this tectonic setting is the Central Andes, one of the world's most Cu–Au productive regions. Porphyry copper deposits are regarded as large magmatic-hydrothermal ore systems, where most key components of these ore mineralizations (i.e., sulfur, metals, and fluids) are sourced from the associated magmas (Sheppard and Taylor 1974; Hedenquist and Lowenstern 1994; Shinohara and Hedenquist 1997; Ballard

et al. 2002; Richards 2003; Dreher et al. 2005; Williams-Jones and Heinrich 2005; Pettke et al. 2010; Simon and Ripley 2011). In other words, the evolution of magmas associated with porphyry copper deposits is thought to exert a first-order control on ore genesis, and thus, it is relevant to assess the magmatic history of these mineralized systems (Chelle-Michou et al. 2015).

Most economic porphyry copper systems from the Central Andes of Chile are intimately associated with major Cenozoic tectonic events (Mpodozis and Cornejo 2012). These tectonic events resulted in episodes of intense deformation, crustal shortening, and thickening, accompanied by the development of the adakite-like geochemical signature (i.e., high Sr/Y, La/Yb, Al_2O_3, and Na_2O; low Mn, Sc, and no Eu* anomaly) in felsic magmas associated with economic-grade mineralizations (Kay et al. 1991; Skewes and Stern 1994, 1995; Kurtz et al. 1997; Rabbia and Hernández 2000; Richards et al. 2001; Kay and Mpodozis 2001, 2002; Ballard et al. 2002; Perelló et al. 2003; Sillitoe and Perelló 2005; Chiaradia et al. 2009; Mpodozis and Cornejo 2012; Loucks 2014).

The origin of the adakite-like signature in magmas associated with porphyry copper deposits from the Central Andes has been attributed to different mechanisms, ranging from slab melting (Oyarzun et al. 2001) to intra-crustal processes (Richards 2002; Rabbia et al. 2002). There is growing evidence, however, suggesting that the high Sr/Y magmas associated with porphyry systems worldwide are not slab melts, instead they may result from magmatic evolution at mid-to-deep crustal levels (see summary in Chiaradia et al. 2012).

Here, we present a petrological study of the magmatic suite associated with the El Abra porphyry copper deposit from northern Chile. This work concentrates mainly on late magmatic events (~39 to 36 Ma) at El Abra, which display a transition from non-adakite to adakite-like geochemistry, where the later adakite-like magmatism is closely related to the ore mineralization (Correa et al. 2016). The new petrological information is then contrasted and complement with that from the older magmatic period (~45 to 40 Ma) at El Abra, available from the previous works (Ballard 2001; Ballard et al. 2002; Haschke 2002; Rojas 2015). Finally, the adakite-like geochemistry is discussed in the middle Eocene–early Oligocene tectonic context of the northern Chile Andes.

Tectonic setting

The El Abra deposit (21°55′S–68°50′W, Fig. 1a) belongs to the late Eocene—early Oligocene metallogenic copper belt of northern Chile, which spans 1400 km between 28° and 31°S, and hosts several world-class porphyry copper deposits (e.g., Quebrada Blanca-Collahuasi, Radomiro Tomic-Chuquicamata, La Escondida, El Salvador) along with numerous small prospects and deposits. It is emplaced in the Precordillera of northern Chile, a region locally known as the Cordillera de Domeyko. It is a rugged, longitudinal mountain range, which represents the western piedmont of the main (Andes) Cordillera. The magmatism spatially associated with the El Abra deposit developed between ~45 and 36 Ma (Correa et al. 2016). This is a period of fundamental changes in the subduction regime in the Central Andes, marked by accelerated westward motion of the South American plate, very high rates of oceanic crust production in the eastern Pacific and strong interplate coupling (Mpodozis and Cornejo 2012).

The Domeyko Fault System, which tectonically controls most of the late Eocene to early Oligocene metallogeny in northern Chile, is a lithospheric-scale, orogen-parallel zone of deformation of more than 1000 km length and 40–60 km width. It is composed of a complex array of strike-slip, normal, and reverse faults, and thin and thick skinned folds and thrusts (Reutter et al. 1991; Mpodozis et al. 1993; Mpodozis and Cornejo 2012). The Domeyko Fault System was developed along the Precordillera of northern Chile as a consequence of compressive tectonic events starting in the Late Cretaceous and ending with the Incaic orogeny when most porphyry copper deposits (43–31 Ma) were formed. During this critical period of ~10 Ma, the final uplift of the Cordillera de Domeyko was produced by differential shortening focused along a mechanically weak crust zones inherited from the Paleozoic (Maksaev and Zentilli 1999; Mpodozis and Cornejo 2012, and references there in). In this period, large plutonic complexes genetically related to several world-class porphyries (e.g., Quebrada Blanca-Collahuasi, Chuquicamata-Radomiro Tomic, La Escondida) were emplaced.

The Chuquicamata-El Abra area (Fig. 1a) is considered an anomalous zone along the Cordillera de Domeyko, where magmatism was recurrent since the Late Cretaceous and where volcanism was almost absent (Mpodozis and Cornejo 2012; Tomlinson et al. 2001; Dilles et al. 1997). The El Abra-Fortuna complex (45–36 Ma) was emplaced in this anomalous zone along the trace of an inverted normal fault inherited from Mesozoic back-arc extension and Quetena reverse fault (Mpodozis and Cornejo 2012). This batholithic complex was finally cut and displaced by 35 ± 1 km to the south by the sinistral movement along the West Fault structure (Fig. 1a, b), which is a significant North–South trending branch of the regional Domeyko Fault System (Dilles et al. 1997, 2011).

Geology of the El Abra district and its surroundings

The geological description presented here is a brief account of major rock units that crop out at an area of

Fig. 1 **a** Topographic map of South America showing the Andean Cordillera in its western margin (from USGS EROS Data Center) and map of the central Andes from 21 to 25°S latitude, including international borders, physiographic-geologic zonation, and structural features. *Black continuous lines along the center of the figure* represent faults from the Domeyko Fault System. *White triangles* represent major volcanic centers from de Central Volcanic Zone (CVZ). Structural and geological data modified from SERNAGEOMIN (Geologic map of Chile, 2002). *Boxed area* shows location of The El Abra deposit in the Precordillera region. **b** District Geology and location of the El Abra open pit (modified from Cornejo et al. 2014) projection: UTM19; Datum—South America Provisional 1956
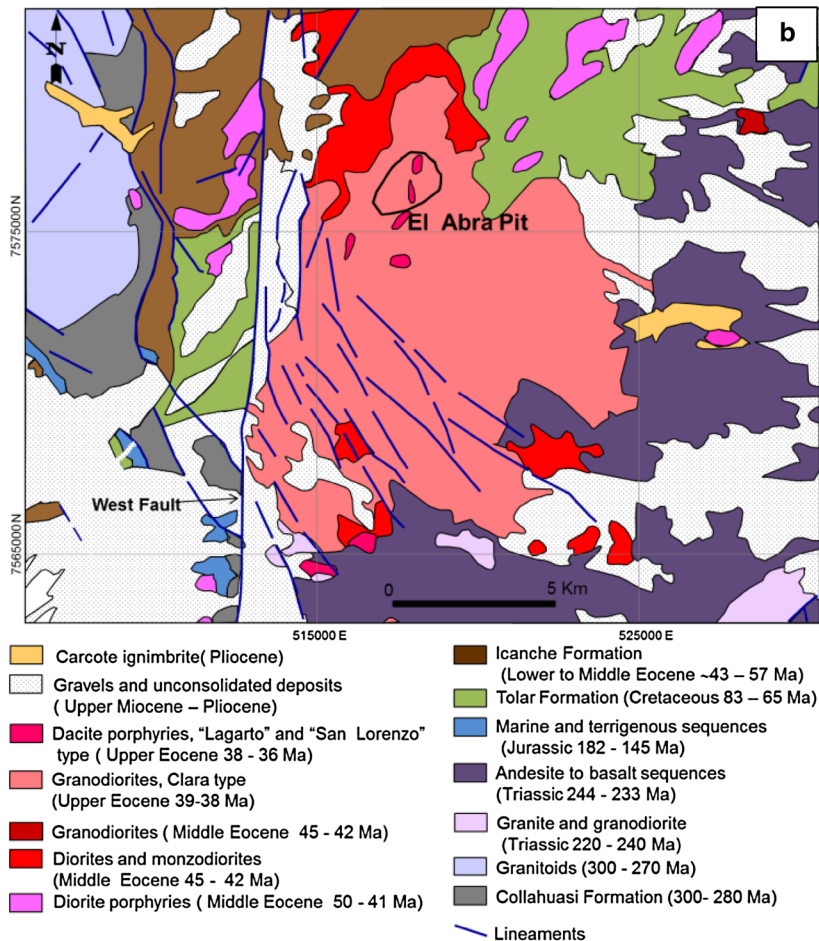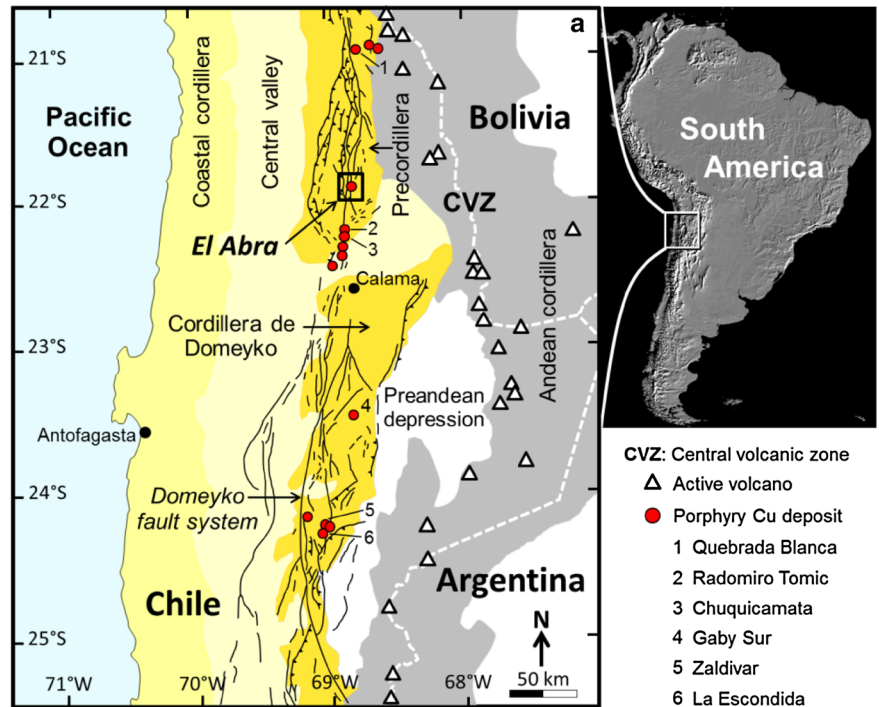
about 30 km × 25 km (Fig. 1a, b) in the El Abra district. The work of many authors over decades has led to some complexity in the rock unit nomenclature of the El Abra district. For a brief discussion on this topic, the reader is referred to Correa et al. (2016). In addition, Table 1 provides a comparison between regional and mine nomenclature for Eocene igneous rocks in the district. This table also includes an up dated list of U-Pb zircon ages for each intrusive rock unit.

The El Abra district is tectonically cut by the West Fault structure (Fig. 1b); consequently, the outcrops on each side of this structure differ. On the west side, the dominant rock

types include: the upper Paleozoic andesites from the Collahuasi Formation and coetaneous granitoids, the Triassic marine and terrigenous sequences, the red beds from the upper Cretaceous Tolar Formation, and the volcano-sedimentary rocks belonging to the lower to middle Eocene Icanche Formation. These units are then intruded by middle Eocene porphyries, and locally covered by the upper Miocene gravels, which represent the youngest rock units in the district (Fig. 1b). On the east side of the West Fault, Paleozoic rock units are absent. Here, other rock types occur including the Triassic andesite to basalt and the Triassic granite to granodiorite intrusive units along with a variety

Table 1 Summary of regional and mine nomenclature and U-Pb ages for igneous rock units from El Abra District

Regional units names	Mine nomenclature	Age (Ma)
Pajonal complex		
Pajonal diorite	None	42.9 ± 0.5^3
		43.21 ± 0.21^5
El Abra granodiorite complex		
Cerro Panizo de Ojuno Qtz-diorite	Dark diorite	40.2 ± 0.5^3
		40.51 ± 0.99^4
		40.83 ± 0.34^5
Abra granodiorite	Central diorite	40.6 ± 0.3^3
		40.62 ± 0.31^4
		40.64 ± 0.25^5
	Equis qtz-monzodiorite	38.5 ± 0.4^3
		41.74 ± 0.19^5
Llareta granodiorite and granite	Rojo Grande granite	38.75 ± 0.61^3
		39.09 ± 0.03^1
		39.14 ± 0.24^5
Clara granodiorite	Clara granodiorite	37.55 ± 0.20^5
		37.82 ± 0.57^2
		37.93 ± 0.42^4
		38.0 ± 0.3^3
		38.71 ± 0.11^1
	Mesocratic Clara granodiorite	37.45 ± 0.09^1
		38.83 ± 0.47^2
Apolo aplites, leucogranite and aplitic porphyries	Apolo aplites, leucogranite and aplitic porphyries	37.55 ± 0.26^5
		38.5 ± 0.4^3
Lagarto granodiorite porphyry	Andesite porphyry	36.89 ± 0.31^5
		37.16 ± 0.38^4
		37.4 ± 0.3^3
		37.49 ± 0.10^1
		38.94 ± 0.65^2
Lagarto mafic granodiorite porphyry	Dacite porphyry	36.07 ± 0.15^1
		38.48 ± 0.62^2

References: [1]Correa et al. (2016) (zircon/CA-TIMS), [2]Correa et al. (2016) (zircon/LA-ICP-MS), [3]Ballard (2001) (zircon/LA-ICP-MS), [4]Campbell et al. (2006) (zircon/LA-ICP-MS), [5]Valente (2008) in Santana (2010) (zircon/LA-ICP-MS). All dates from Correa et al., 2016 are from the pit site. Note that samples EA-561 and EA-1284 from El Abra prophyry dated by Correa et al. (2016) were originally classified as dacite and rhyolite, respectively, based on chemical information (see TAS diagram, Fig. 8b) but re-classify in this work as andesite and dacite porphyries, respectively, based on available modal analyses (online resource ESM_2)

of granitoids from the Eocene Pajonal and El Abra igneous complexes (Table 1). These Eocene igneous complexes become the dominant outcrops in the district, covering about 50% of the area (Figs. 1b, 2). Among these intrusive rock units, the Clara granodiorite is the largest one, with a sub-circular outcrop of about 12 km in diameter (Tomlinson et al. 2001). A few younger (post-mineralization) units including the Carcote Ignimbrite (Pliocene), as well as consolidated and unconsolidated gravels and alluvium (Fig. 1b) complete the surface geology of the east part of the district (Barrett 2004; Tomlinson et al. 2001; Cornejo et al. 2014).

At the mine site, the late Eocene intrusive rocks belonging to the El Abra Granodiorite Complex (Fig. 2) dominate, which is part of the Pajonal-El Abra Complex at district scale (Table 1). Here, the El Abra Granodiorite Complex is mainly represented by the older Central diorite, Equis quartz monzodiorite, and Dark diorite cropping out chiefly at the central and western sectors of the open pit (Fig. 2). In addition, subordinated outcrops of the Rojo Grande granite are present at the northeast sector of the mine (Fig. 2). All these rocks, which are the main host of the copper mineralization at El Abra, are granitoids with medium-grained equigranular texture. These rock units intrude the slightly older Pajonal Igneous Complex in the northern fringe of the open pit, and are in turn intruded by younger units from the El Abra complex, including the Clara granodiorite, Apolo granite-aplite, and the El Abra porphyries and their associated breccias (Fig. 2). At the mine site, the outcrop of Clara granodiorite is restricted to the south-east corner of the open pit. This is a medium grained equigranular to slightly porphyritic rock that on surface is poorly mineralized, but at depth, it is the main host rock of the mineralization. Large (up to 30 m) and narrow (less than 1 m wide) aplites and phenocryst-poor aplitic dikes cut the Clara granodiorite mainly in its northern and western borders, while pegmatite dykes cut across the southern part of Clara granodiorite. These late intrusions were denominated 'aplitic granite porphyry' by Dilles et al. (1997) and include the Apolo leucogranite and the aplite-pegmatite unit. The youngest unit of the El Abra complex is the El Abra porphyry, which occurs as dikes and irregular intrusions within the central zone of the open pit. At district scale, the equivalent rock units to the El Abra porphyry are the main Lagarto granodiorite porphyry and the late Lagarto mafic granodiorite porphyry (Dilles et al. 1997; Tomlinson et al. 2001). These dykes consist of several intrusive events emplaced at slightly different times. Additional textural varieties of these porphyritic dykes have also been intercepted at depth (~1 km below surface) by a deep drilling program carry out at the mine site (Ardila 2009). Two varieties of these porphyry dykes found at depth were dated by zircon U/Pb CA-TIMS method (Table 1), defining a ~1.4 Ma period of porphyry intrusion, which is coeval with the main Cu-Mo mineralization period (Correa et al. 2016).

Alteration and mineralization

The main alteration zones at El Abra include a potassic core surrounded by a quartz-sericite zone. An albite-tourmaline

Fig. 2 Geology of the El Abra deposit. Projection: UTM19; Datum: 1956 Provisional South America. SCMEA internal report
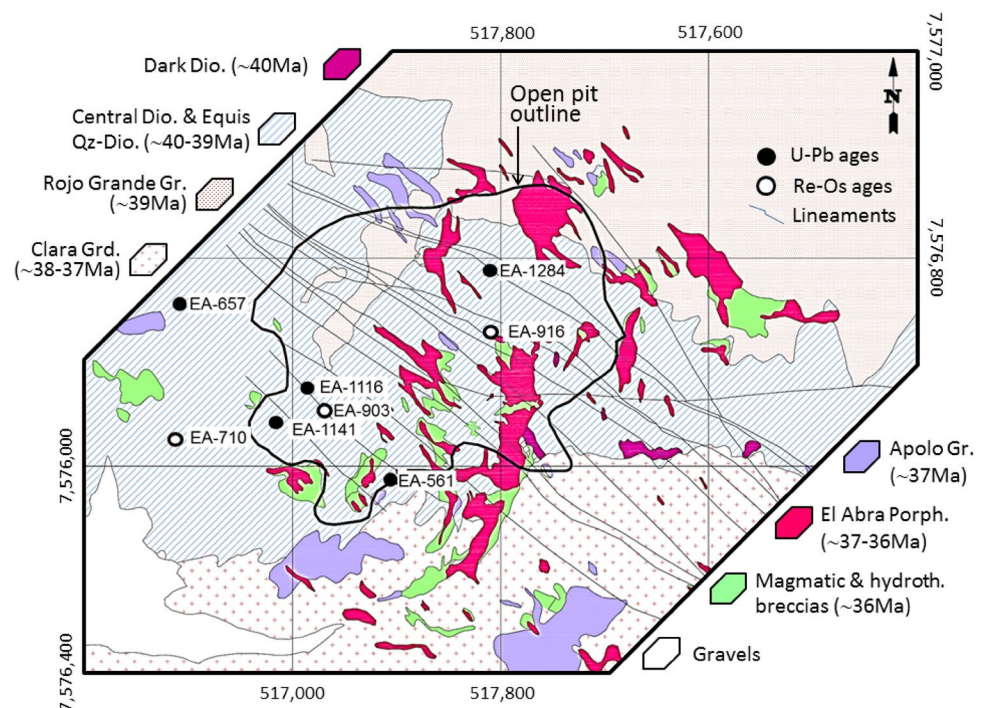
alteration zone is present at depth in the western and southwestern sectors of the open pit. Finally, a poorly developed propylitic envelope extends outwardly from the quartz-sericite zone.

In the potassic core zone, developed at the central and deeper parts of the mine, bornite + chalcopyrite ± magnetite associations prevail, followed by chalcopyrite > bornite ± molybdenite, with chalcopyrite > pyrite ± molybdenite dominant in the outer portions of the orebody. The albite-tourmaline alteration is mostly restricted to small breccias and dikes. Tourmaline occurs either as thin veinlets with an albitic halo or as breccia matrix with scarce sulfides (pyrite-chalcopyrite). The quartz-sericite zone occurs mainly related to hydrothermal breccias and zones associated with northwest-trending structures (D veinlets infilled with quartz—chalcopyrite ± bornite ± pyrite ± molybdenite) and is associated with the main structural trends in the southeast part of the district (Ardila 2009).

Molybdenite Re–Os geochronology defines a restricted mineralization episode with a mean ore formation age of 36.25 ± 0.25 Ma (Correa et al. 2016), which is temporally and spatially associated with the El Abra porphyries and igneous-hydrothermal breccias emplacement.

Methodology

A sampling protocol to obtain information on the magmatic history of the El Abra magmatism aimed at mitigating the effects of hydrothermal alteration on mineralogy was used. This includes avoiding sampling areas with pervasive destructive alteration (e.g., quartz-sericite), highly fractured or brecciated zones and eliminating veins and alteration halos when present in hand samples. In addition, to avoid visible alteration in samples selected for geochemical analyses, the whole rock pieces were handpicked after the crushing and prior to the pulverizing stage.

Thirty-five drillholes of ~2000 m length from the deeper (800–2000 m) parts of the deposit were reviewed, focusing on intrusive units related to hypogene mineralization. The most representative samples of each unit were chosen for petrographic, geochemical, and isotopic analysis. Detailed petrography of the samples was done by a combination of optical microscopy and scan field analysis using automatized mineralogy analysis performed by QEMSCAN. Plagioclase compositions were determined using a JEOL JXA8600 electron microprobe equipped with five wavelength-dispersive spectrometers, at the Institute of Applied Economic Geology, University of Concepcion, Chile. The analytical conditions were as follows: 15 kV accelerating voltage, a beam current of 20 nA for major elements (Si, Al, Ca, and Na) and 40 nA for minor elements (K, Sr, Mg, Fe, and Ba), a spot size of

10 μm and counting times of 10–40 s for major elements, and 60–140 s for minor elements, on peak and half this time on the respective backgrounds. Strontium was measured with a PET crystal to avoid Si $K\alpha$ overlap on the TAP crystal. Both natural and synthetic silicates and glasses were used as standards for calibration. Standards were synthetic wollastonite (Ca), forsterite (Mg), sanidine (Si, K), jadeite (Na), celestite (Sr) and Ba–Zn glass (Ba), and natural anorthite NMNH 137041 and fayalite NMNH 85276 from the Smithsonian Institution (Al and Fe, respectively). Analytical precisions were better than ~1% for elements above 10 wt% oxide, ~5% at 1–10 wt%, and ~10% at levels <1 wt%. Detection limits for K, Sr, Ba, and Fe measured in plagioclase are: 77, 195, 480, and 289 ppm, respectively. Data reduction was performed using the ZAF correction method. Selection of points for analysis was done using backscattered electron images.

Whole rock major and trace elements were analyzed using a combination of FUS-ICP, FUS-MS; TD-ICP, and INNA at Activation Laboratories Ltd. (Canada) for a total of 30 samples. In addition, seven samples were analyzed for Sr–Nd–Pb using a six-collector solid source mass spectrometer (Finnigan-MAT) at the Cooperative Institute for Research in the Environmental Sciences, University of Colorado (USA).

The LA-ICP-MS analyses of mineral phases were performed at the Department of Earth Sciences, Laurentian University (Canada). The instrument consisted of a Thermo XSeries 2 quadrupole ICP-MS and a 193 nm Excimer laser from Resonetics. The analysis mode was set to spot analysis. The spot size used was 32 μm, and the ablation rate was 5 Hz. On larger mineral grains, multiple spot analyses were made on the same grain. The external calibration standard was NIST611 glass that contains nominal element concentrations between 400 and 500 ppm for over 40 elements. External calibration standards (MP-DING glasses; Jochum et al. 2006) were analyzed with the same experimental conditions as the samples at the beginning and at the end (usually after 10–15 unknowns) of the experiment. Analysis time ranged between 45 and 60 s, including 25 s of background acquisition and 20–25 s of ablation time. In the database, only the elements that resulted in detectable concentrations are reported. The quantification of absolute concentration values requires an internal standard element for each mineral phase. This internal standard element is determined by an independent method, EMPA in this case. The output raw was processed using the software 'Iolite' (Hellstrom et al. 2008). The data processing included the selection of an appropriate portion of the signal for integration and choosing the internal standard element concentration. Detection limits were calculated as three times the standard deviation of the background of the gas blank.

Results

Petrography of intrusive rocks

A synthesis of the petrography from older to younger rock units intercepted at depth at the mine site is presented. For a description of the older Central diorite, Equis quartz monzodiorite and Dark diorite, not included here, it is referred to Ballard (2001); Tomlinson et al. (2001) or Barrett (2004). Figure 3 shows the QAP classification results of analyzed rocks. Additional textural and mineralogical descriptions for each rock unit can be found as online resource (ESM_1). This petrographic information of rocks sampled at depth (800–2000 m) complements the surface geology of the El Abra deposit (see above).

Rojo Grande granite (EA-661 and EA-657)

This unit appears as a medium grained equigranular monzogranite (Figs. 3, 4a, b) with a color index (i.e., sum of volume percentages of the dark or colored minerals) (CI) of 5.5–7.4 and with biotite as the main ferromagnesian mineral (online resource ESM_2). This unit contains minor chalcopyrite (10–20 μm in size) homogeneously disseminated, but abundant Cu mineralization as sheeted veins and strong stockworks with bornite–digenite–chalcopyrite near the contacts with younger porphyritic units and hydrothermal breccias. Cu mineralization is low at depths greater than 1000 m. Common accessory minerals include zircon, titanite, apatite, and magnetite (online resource ESM_2).

Clara granodiorite (EA-1099, EA-1141, EA-1359, EA-860, and EA-1210)

This unit appears as a coarse-grained equigranular, locally porphyritic, granodiorite to leuco-quartz-monzodiorite (Figs. 3, 4c, d, e, f) with a CI of 6.1 to 11.6. Biotite dominates over amphibole (online resource ESM_2). At surface, this unit exhibits poor mineralization mostly represented by disseminated chalcopyrite (30–40 μm in size). At depth, however, it is the main host rock for Cu mineralization present as thin A- and AB-type (quartz-rich) veinlets with bornite–digenite–chalcopyrite ± anhydrite. Mineralization is mainly concentrated near the contacts with younger porphyry bodies. This unit locally contains small (<4 cm) subrounded mafic inclusions of quartz-diorite composition, probably representing cognate xenoliths. Typical accessory minerals include zircon, sphene, apatite, and magnetite (online resource ESM_2).

Mesocratic Clara granodiorite (EA-1116)

Intercepted at 1 km depth from the pit level. This rock type shows meso- to melanocratic bands (less than 50 cm wide) and no clear contacts with the main Clara granodiorite. It is a coarse-grained equigranular rock with a granodiorite composition and a high, but variable CI generally >20 (Figs. 3, 4g, h). The presence of large (up to 20 mm) and euhedral hornblende crystals is a characteristic feature of this rock type. Modal abundance of hornblende and biotite is high, 11–18 and 8–12 vol%, respectively. Cognate xenoliths of biotitized diorite (Dark or Central diorite?) are locally present. Mineralization is observed as disseminated chalcopyrite around quartz-rich A-type and AB-type veinlets, which are filled with potassium feldspar, together with abundant anhydrite and bornite-chalcopyrite. Typical

Fig. 3 QAP classification diagram using modal count from QEMSCAN analyses
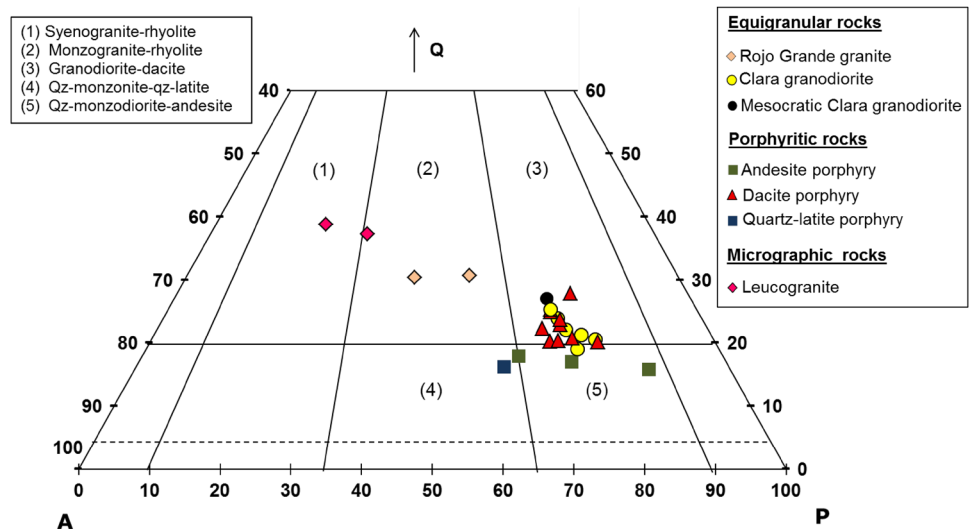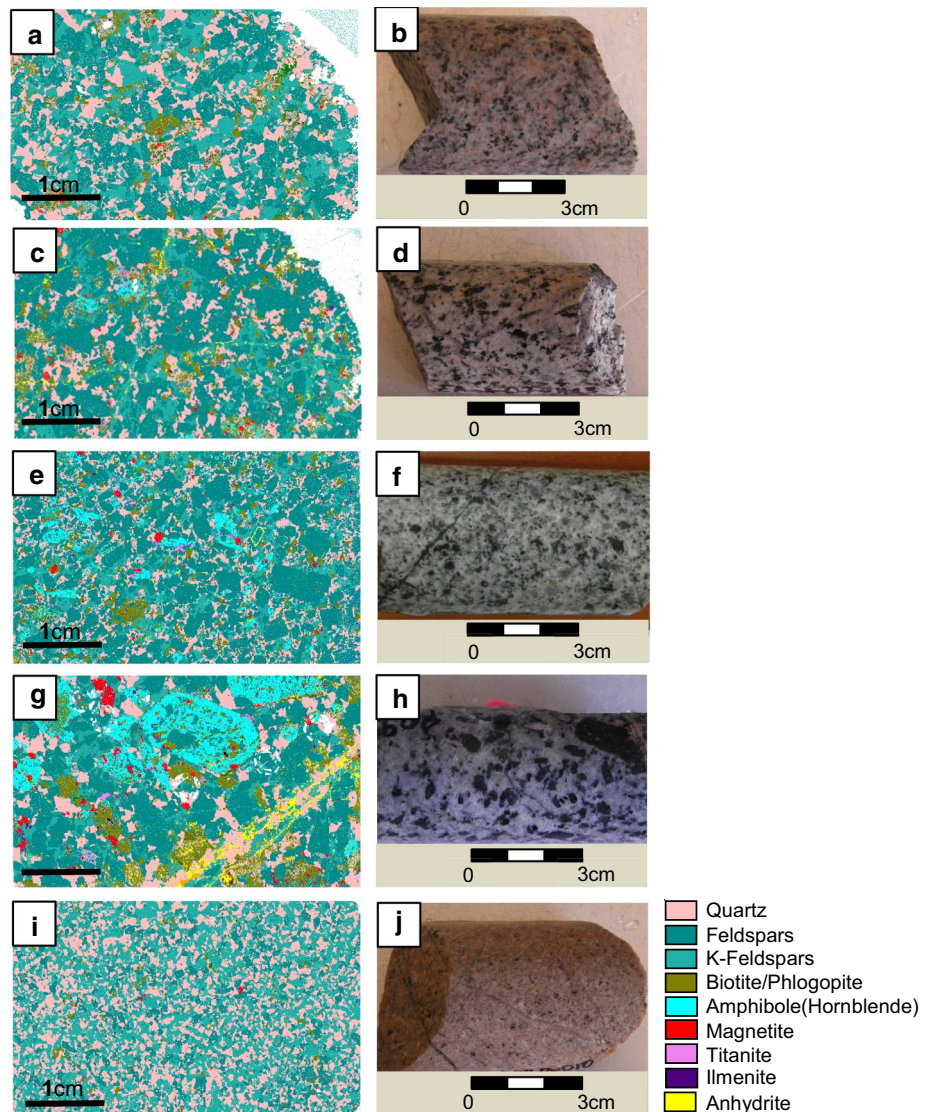
Fig. 4 Selected QEMSCAN false-color images of textures and mineral composition of the El Abra rock samples from different units: **a, b** Rojo Grande granite (EA-657). **c, d** Clara granodiorite (EA-1141). **e, f** Porphyritic Clara granodiorite (EA-1099). **g, h** Mesocratic Clara granodiorite (EA-1116). **i, j** Leucogranite (EA-447)

Quartz
Feldspars
K-Feldspars
Biotite/Phlogopite
Amphibole(Hornblende)
Magnetite
Titanite
Ilmenite
Anhydrite

accessory minerals include zircon and abundant sphene, apatite and magnetite (online resource ESM_2).

El Abra porphyry

Given the fine-grained nature of the groundmass of these rocks, a volcanic terminology is adopted for their classification. Accordingly, these rocks are sub-divided into the following compositional categories: andesite porphyry, dacite porphyry, and quartz-latite porphyry.
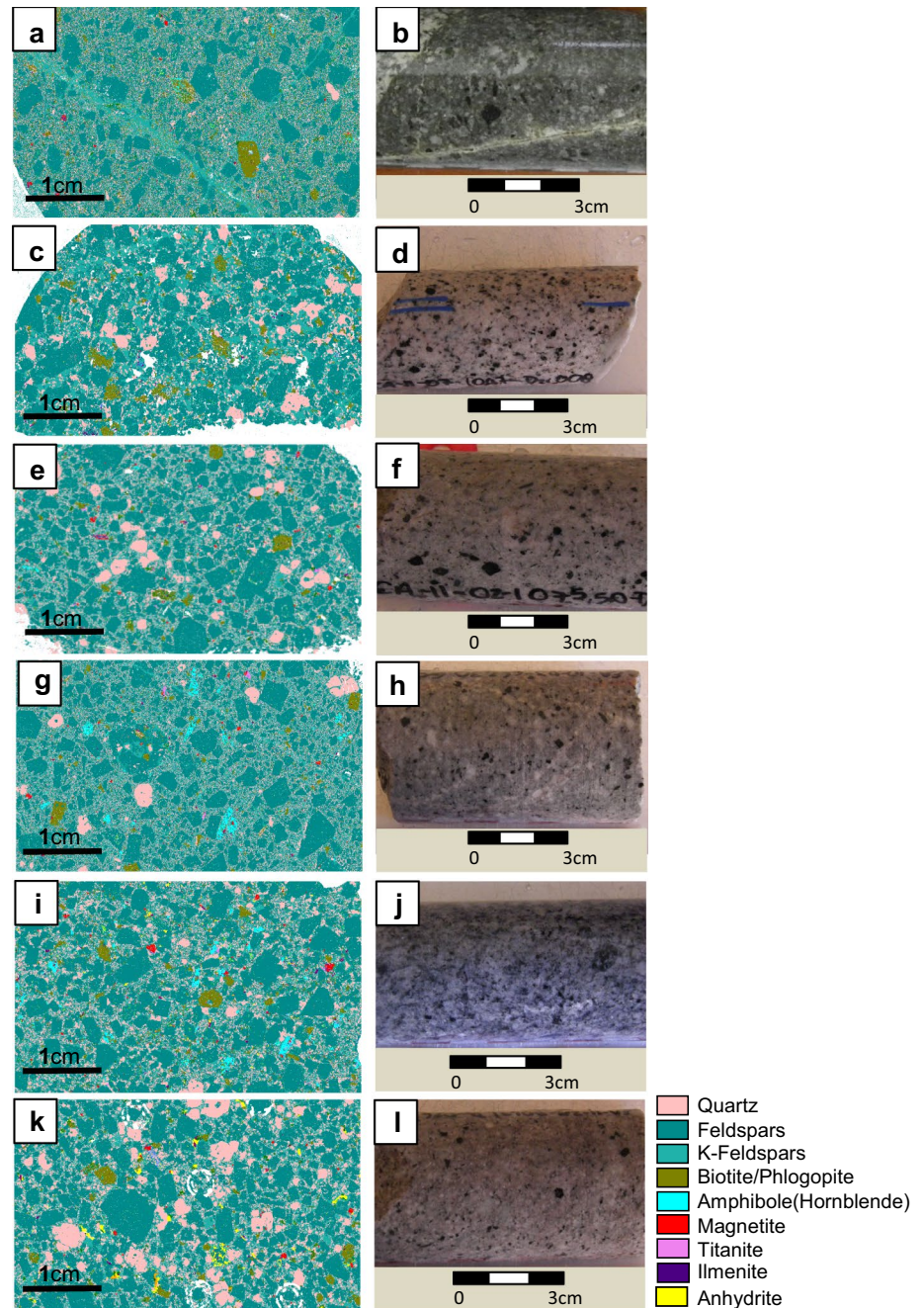
Andesite porphyry (EA-651, EA-561, and EA-1047)

These samples plot in the andesite field of the QAP diagram (Fig. 3). They are leucocratic (CI <15) with porphyritic texture (~57–76 vol% of phenocrysts) (online resource ESM_2) and a fine-grained groundmass (200–600 μm)

(Fig. 5a, b). Biotite is more abundant than amphibole (online resource ESM_2) and dominates in the groundmass.

Disseminated bornite, chalcocite, digenite, and chalcopyrite occur in samples EA-651; EA-561. Myrmekite-like texture between bornite–chalcocite is also locally observed in these samples. Andesite porphyries are crosscut by quartz-rich veinlets with biotite–bornite–chalcopyrite and K-feldspar halos. Similar quartz-rich veinlets with less biotite and more digenite are found in sample EA-1047. In addition, dissemination of bornite–digenite (70–150 μm in size) and chalcopyrite (10–20 μm in size) associated with hematite–magnetite are disseminated close to veinlets.

At the deposit site, these rocks are volumetrically minor. They are commonly present as dykes intruding Clara granodiorite but also as small cognate inclusions (autoliths) in dacite porphyry rocks. Typical accessory minerals include zircon, sphene, apatite, and magnetite (online resource ESM_2).

Fig. 5 False color QEM-SCAN images of textures and photographs of intramineral Abra porphyries. Andesite porphyries: **a, b** (EA-561); **c, d** (EA-1047). Dacite porphyries: **e, f** (EA-1075); **g, h** (EA-662); **i, j** (EA-1535); **k, l** (EA-901)

Quartz
Feldspars
K-Feldspars
Biotite/Phlogopite
Amphibole(Hornblende)
Magnetite
Titanite
Ilmenite
Anhydrite

Dacite porphyry (EA-874, EA-247, EA-1535, EA-1086, EA-1075, EA-1203, EA-662, EA-1284, EA-862, and EA-901)

This is the most abundant type of porphyry in the open-pit area. These samples plot in the dacite field of the QAP diagram (Fig. 3). Most of these porphyritic rocks are leucocratic (CI<5) with variable amounts of phenocrysts (~47–70 vol%) (online resource ESM_2), having a microfelsic groundmass (50–400 μm in size) (Fig. 5c–l). Biotite is typically more abundant than amphibole in these

porphyries. In some samples (EA-862, EA-1284, and EA-901) quartz aggregates are common (quartz eyes). Locally, this unit gradually changes from coarse porphyry texture to a micrographic texture passing to a leucogranite (e.g., samples EA-447 and EA-577). Typical accessory minerals include zircon, sphene, apatite, and magnetite (online resource ESM_2).

Stockworks or sheeted veins are common near the contact of the dacite porphyries. These are composed of quartz-rich A and AB-type veinlets, with associations of biotite ± anhydrite ± bornite ± digenite ± chalco-

pyrite ± molybdenite ± pyrite and B veinlets filled with quartz ± bornite < chalcopyrite and with discontinuous K-feldspar halos. All these veins are crosscut by late D veinlets with chalcopyrite and quartz-sericite halos with disseminate chalcopyrite.

Quartz-latite porphyry (EA-660)

This rock is a leucocratic (CI < 10) quartz-monzonite with porphyritic texture (37 vol% of phenocrysts). Fine-grained phenocrysts (200–600 μm) of partially sericitized plagioclase are set in a very fine-grained groundmass (20–80 μm) dominated by plagioclase, quartz, and potassic feldspar (online resource ESM_2). Biotite and amphibole partially altered to chlorite-epidote are the main ferromagnesian phases (online resource ESM_2). Zircon, sphene, magnetite, and apatite are the main accessory minerals. Mineralization is scarce and largely represented by disseminated chalcopyrite and pyrite in the groundmass. This rock forms a series of late polymict igneous breccias (Fig. 6a) that can be observed towards the south of the current open pit.

Leucogranite (aplite) (EA-447, EA-577)

This aplite unit is technically a leucogranite (CI < 5) with a very few subrounded quartz and plagioclase phenocrysts (up to 3 mm) (Fig. 4i, j; online resource ESM_2). Samples EA-447 and EA-577 intrude the Clara granodiorite as small dikes (up to ~3 m), which are larger, however, than the typical leucogranite dikelets (<30 cm in wide) that usually appear cutting the porphyritic varieties of El Abra porphyry. The precise age of these larger intrusions is not known.

The leucogranite dikelets locally show unidirectional solidification textures, characterized by quartz and K-feldspar intergrowths, monomineralic bands of crenulated quartz and K-feldspar intercalated with aplitic material (Fig. 6b, c) and locally forming a poorly developed "brain rock" (Shannon et al. 1982) to the edge of large dykes. These bands with unidirectional solidification textures vary in size from 0.5 to 3 cm and contain miarolitic cavities. Locally, fine-grained bornite seems to delineate the borders of these thin dykes. Quartz-rich (A and B-type) veinlets are observed with bornite, digenite and chalcopyrite. These veinlets are frequently re-used by late D type veinlets with chalcopyrite and molybdenite. Disseminated mineralization is also observed as bornite–digenite association replaced by covellite and chalcopyrite.

Multiple leucogranite phases are identified at El Abra. The earliest leucogranite porphyry phase with plagioclase phenocrysts and aplitic matrix intrudes the Clara granodiorite at ~800 m depth. This intrusion is cross-cutting early A and B veinlets in the Clara granodiorite and is cut by
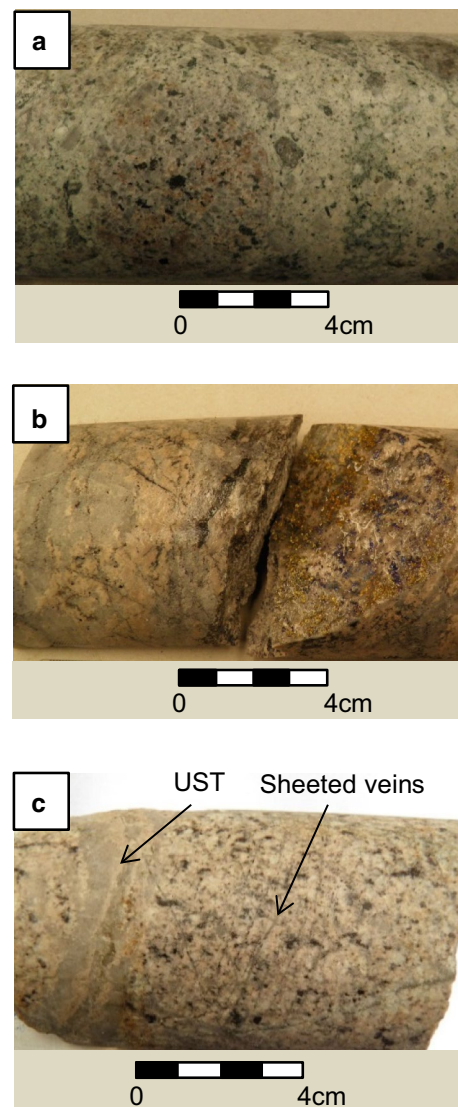
Fig. 6 a Polymict igneous breccia, matrix: late quartz-monzonite porphyry. **b, c** Comb-quartz-layers and UST textures in leucogranite samples

late B and D veinlets. Clasts of leucogranite are also found in dacite porphyries and magmatic breccias with a matrix of dacite porphyry. The most frequent association of leucogranites is with the most evolved varieties of the dacite porphyry.

Plagioclase micro-textures and mineral chemistry

To complement the petrographic and geochemical information, the composition of plagioclase from selected samples was determined. The results are available as online resource (ESM_3). A synthesis of plagioclase compositions is presented in the following.

Clara granodiorite (EA-1099)

This sample represents a porphyritic coarse-grained variety of Clara granodiorite (38.71 Ma; Correa et al. 2016). The An content of large phenocryst cores (800–1000 μm in size) varies from An28 to An34; oscillatory zoning domains with irregular resorption zones, where more calcic plagioclase (An40–An48) is present, are characteristic of these plagioclase phenocrysts. Calcium increase in these resorption zones is decoupled from Sr and Fe contents, which remains relatively constant In the entire crystal, the Sr and Fe concentrations show only minor variations, between ~1000 and 1200 ppm for Sr and from ~800 to 1200 ppm for Fe, respectively, and commonly do not correlate with the An content. An exception is present in a groundmass grain with high An content (An56), where Fe yields 4115 ppm. In these large phenocrysts, An content decreases towards the rims (An19–An24), together with as the minor and trace elements. Groundmass plagioclase presents cores with variable An content (An25–An63) and with dissolution and patchy textures.

Dacite porphyries (EA-874, EA-662)

Among the dacite porphyries, these samples represent the older ones (37.49 Ma; Correa et al. 2016). Plagioclase phenocrysts from these samples also contain sodic cores (An29–An36) with 1140–1800 ppm of Sr and 1100–1700 ppm of Fe, respectively. Although not present in all grains, dissolution (patchy) texture is followed by zones with fine scale oscillatory zoning or resorption surfaces. The last are followed by more calcic zones (An31–An53), where Sr and Fe increase about 100 ppm and up to 500 ppm, respectively. This increase in An, Sr, and Fe contents is less marked in some crystals. The Sr, Fe, and An contents decrease towards the rims (Sr <1200 ppm; Fe <900 ppm, and An7–An21).

Dacite porphyry (EA-1284)

This sample represents the latest porphyritic event (36.07 Ma; Correa et al. 2016). Plagioclase phenocrysts from this sample are characterized by large cores (1400 μm) with An21–An30; 1100–1700 ppm of Sr and 700–1380 ppm of Fe, respectively. Some grains show multiple resorption surfaces, where An, Sr, and Fe contents are elevated (An35–An42; Sr 1800–2000 and Fe 900–1500 ppm). These surfaces are followed by fine scale oscillatory zoning with composition similar to the core. Medium-sized phenocrysts (900–1000 μm) present rounded cores with wavy fine scale oscillation zoning. Contents in An varies between An23 and An35, Sr between 1193 and 1699 ppm and Fe between 880 and 1381, where

the highest content of minor elements is present in the core and tends to decrease towards the rim. The rims of these plagioclase phenocrysts have An12–An19; Sr <800 ppm and Fe <700 ppm.

Geochemistry

Hydrothermal alteration effects on whole rock geochemistry

Despite the precautions taken during sampling and sample preparation (see "Methodology"), the hydrothermal alteration was not completely eliminated in some samples. In particular, those rocks with potassic alteration may still exhibit localized areas with pervasive replacement of plagioclase by K-feldspar, recrystallization of biotite phenocrysts, formation of aggregates of biotite intergrown with magnetite replacing hornblende ("shreddy" biotite), and sphene breakdown into rutile along with dissemination of fine-grained biotite in the groundmass of some porphyries. Sodic-(calcic) alteration developed at deep intrusive contacts is superimposed on potassic alteration.

To evaluate the effects of the presence of veinlets associated with potassic alteration, two samples of a dacite porphyry (sample EA-984A and B), one with and the other without (vein material removed by hand-picking) veinlets were analyzed. Figure 7 shows the results of these analyses. The main observed changes include an increase in Cs, Rb, and K, along with SiO_2, and a general concentration decrease of all the remaining elements (Fig. 7a, b; Table 2 and online resource ESM_4). No significant difference in the shape of REE distribution patterns was observed (Fig. 7b), but a dilution of about 18 wt% in the overall abundance of REE is noted (online resource ESM_4). Assuming that the sample (EA-984A) with veinlets material removed by hand-picking represents a less altered composition, closer to the original one, a general dilution effect, due to Si and K addition by veining, appears to be the major chemical modification of this sample. However, the partial sphene replacement by rutile, which is also related to the potassic alteration event, occurs outside the veins of this sample, and thus, the removal of veinlets does not allow quantifying the potential REE mobilization (i.e., rutile has very low REE contents compared to sphene). Despite this mineral replacement may imply a REE mobilization, the scale of this process it is not known (i.e., if it exceeds a hand sample).

Major and trace elements results

Results of major element analyses on anhydrous basis are reported in Table 2. Samples from the El Abra intrusive complex show a calc-alkaline, metaluminous affinity,
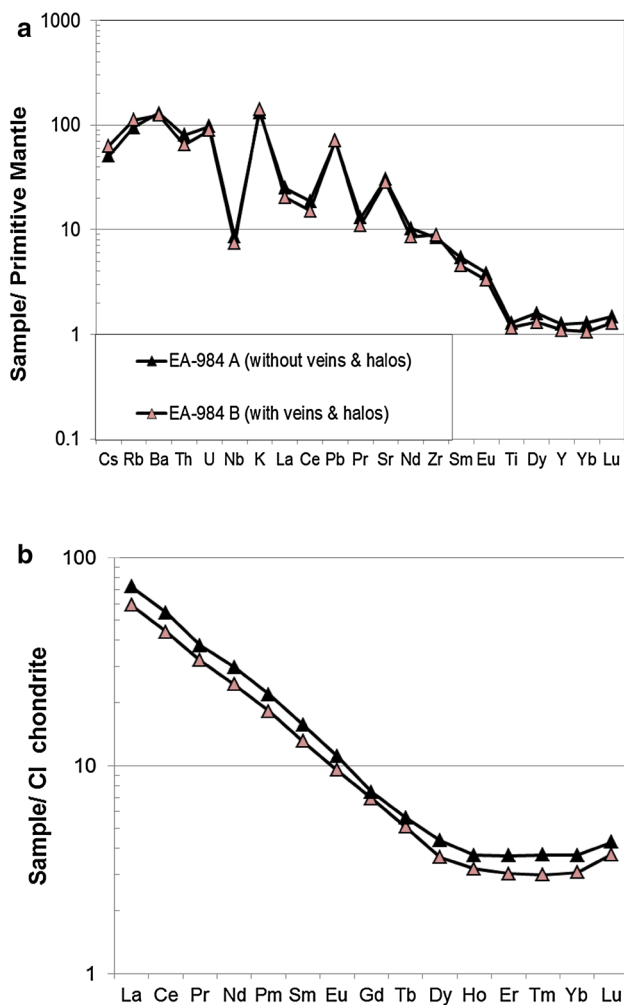
Fig. 7 Comparison of chemical analyses of El Abra dacite porphyry using two sub-samples from sample EA 984, where one part was analyzed without eliminating the altered sectors (veinlets and halos of strong potassic alteration), and in the other part, the alteration and vein material was removed. **a** Spidergram with normalized values to Primitive Mantle (Sun and McDonough 1989). **b** Rare earth elements distribution diagram with normalized values to CI-chondrite Sun and McDonough (1989). Promethium (Pm) is interpolated between Nd and Sm

have medium-to-high potassium content and relatively high sodium content, particularly the Clara granodiorite and the late porphyries (Fig. 8a–d). The SiO_2 composition of intrusions ranges from about 61 to 78 wt% (Table 2). The SiO_2 content of porphyritic samples, considered in terms of volcanic rock classification, ranges from dacite to rhyolite (Fig. 8b). The Harker diagrams show, with the exception of the two amphibole-rich rocks (samples EA-1116 and EA-775) from the mesocratic Clara granodiorite, a trend similar to that expected for a differentiation process due to crystal fractionation (Fig. 9). However, there is no relationship between age and the degree of evolution, as shown by the progression from the El Abra porphyry (sample

EA-561), with an age of 37.49 ± 0.10 Ma (Correa et al. 2016) and 63.33 wt% of SiO_2 (Table 2), to Clara granodiorite (sample EA-1141), with an age of 38.71 ± 0.11 Ma (Correa et al. 2016) and 65.72 wt% of SiO_2 (Table 2), to Rojo Grande granite (sample EA-657), with an age of 39.09 ± 0.03 Ma (Correa et al. 2016) and 69.66 wt% of SiO_2 (Table 2), where the oldest intrusive units are among the most chemically evolved rocks (Fig. 9).

The El Abra porphyries and Clara granodiorite (64–71 wt% SiO_2) have similar high contents of Sr ~600–900 ppm (Fig. 10, online resource ESM_4). The content of Y, however, is lower in the younger, more differentiated porphyritic rocks (≤ 8.9 ppm), with the exception of sample EA-247 (online resource ESM_4) affected by argillic alteration (online resource ESM_2), than in the Clara granodiorite (≥ 8.5 ppm) yielding higher Sr/Y ratios (~90 and 140; mean ~115) in the porphyries compared to the Clara granodiorite (~60 and 85; mean ~70) (Fig. 10). Although a difference between the intra-mineral El Abra porphyries and Clara granodiorite exist, compared to older rock units they share similar rare earth elements (REE) distribution patterns to the Clara granodiorite, e.g., strongly fractionated (La/Yb 17–36) and without europium anomalies (Eu/Eu* 0.78–0.97), (Figs. 10, 11).

On the other hand, low Sr/Y ratios characterize the leucogranite (Sr/Y ~10), mesocratic Clara granodiorite (Sr/Y ~20) and Rojo Grande granite (Sr/Y ~25) due to a combination of low Sr (<490 ppm) and relatively high Y (>~12 ppm) contents in these rocks (Fig. 10, online resource ESM_4). Regarding the REE, the Rojo Grande granite and the leucogranite have less fractionated distribution patterns (La/Yb 11–23) and a strong negative europium anomaly (Eu/Eu* 0.35–0.58) (Figs. 10, 11). The REE distribution patterns of the mesocratic Clara granodiorite samples (La/Yb ratio of ~16–18) are similar to those from the Clara granodiorite, but the total REE contents are higher and display a negative europium anomaly (Eu/Eu* 0.49–0.61) similar to Rojo Grande granite and leucogranite samples (Figs. 10, 11).

Sr–Nd–Pb Isotopes results

The Sr, Nd, and Pb isotopic ratios of selected samples are presented in Table 3. The ratios for $^{87}Sr/^{86}Sr_i$ range from 0.704541 to 0.704578 for most rock units with the exception of the leucogranite, which is slightly more radiogenic having a $^{87}Sr/^{86}Sr_i$ ratio of 0.704890. The $^{143}Nd/^{144}Nd_i$ ratios for all samples range between 0.512618 and 0.512642. The initial $^{206}Pb/^{204}Pb$, $^{207}Pb/^{204}Pb$, and $^{208}Pb/^{204}Pb$ isotopic ratios also show a limited variation, ranging between 18.09 and 18.54, 15.57 and 15.62, and 38.08 and 38.46, respectively.

**Table 2** Whole rock major oxides (anhydrous base) in weight percentage

Analysis method	FUS-ICP										
Analyte symbol	SiO$_2$	Al$_2$O$_3$	Fe$_2$O$_{3(t)}$	MnO	MgO	CaO	Na$_2$O	K$_2$O	TiO$_2$	P$_2$O$_5$	Total
Unit symbol	wt%	wt%	wt%	wt%	wt%	wt%	wt%	wt%	wt%	wt%	wt%
Detection limit	0.01	0.01	0.01	0.001	0.01	0.01	0.01	0.01	0.001	0.01	0.01
Rojo Grande granite											
EA-661	71.57	14.87	2.18	0.031	1.05	2.23	3.30	4.33	0.350	0.10	100.01
EA-657	69.66	15.48	3.06	0.026	1.33	2.62	3.45	3.83	0.412	0.12	99.99
Clara granodiorite											
EA-1210	65.93	16.82	3.76	0.051	1.47	4.05	4.16	3.08	0.500	0.16	99.97
EA-1359	65.43	16.85	3.77	0.049	1.55	4.58	4.36	2.71	0.509	0.19	99.99
EA-1141	65.72	16.82	3.50	0.041	1.57	4.22	4.48	2.94	0.527	0.19	100.01
EA-866	66.42	16.43	3.33	0.027	1.61	4.16	4.27	3.03	0.525	0.19	99.99
EA-285	66.29	16.97	3.78	0.044	1.60	3.65	4.14	2.84	0.515	0.18	100.01
EA-860	65.13	17.28	4.11	0.031	1.75	4.05	4.28	2.58	0.588	0.20	99.99
EA-1099	64.91	17.04	4.06	0.051	1.68	4.51	4.43	2.57	0.550	0.20	99.99
Mesocratic Clara granodiorite											
EA-1116	60.74	13.99	8.55	0.155	4.27	4.99	3.47	2.49	1.008	0.35	100.02
EA-775	61.28	13.04	10.23	0.091	4.05	3.85	2.70	2.84	1.398	0.50	99.98
El Abra porphyry											
EA-1203	69.73	16.25	2.26	0.029	0.97	2.63	4.39	3.29	0.329	0.14	100.02
EA-662	69.26	16.35	2.28	0.043	0.92	3.00	4.68	2.98	0.345	0.15	100.00
EA-1086	68.22	16.89	2.56	0.040	0.77	3.46	4.83	2.76	0.342	0.13	100.00
EA-1075	68.30	16.99	2.50	0.041	0.80	3.28	4.72	2.85	0.334	0.14	99.96
EA-1770	67.62	16.75	2.94	0.033	0.92	3.77	4.79	2.63	0.372	0.16	99.99
EA-687	68.02	16.81	2.72	0.043	0.80	3.73	4.75	2.62	0.364	0.15	100.00
EA-1047	67.37	17.22	0.98	0.011	1.04	3.83	4.82	4.15	0.405	0.19	100.01
EA-814	67.32	16.99	2.68	0.026	1.02	3.70	4.93	2.78	0.389	0.16	100.01
EA-1535	66.45	17.08	3.28	0.043	1.16	4.06	4.71	2.61	0.439	0.18	100.01
EA-247	64.98	18.64	4.31	0.041	1.53	3.13	4.54	2.00	0.581	0.23	99.99
EA-561	63.33	17.83	4.37	0.046	2.19	4.51	5.01	1.81	0.637	0.28	100.00
EA-874	64.83	18.20	3.90	0.030	1.60	4.04	4.78	1.84	0.543	0.23	99.99
EA-862	69.68	16.28	2.12	0.018	0.68	2.99	4.67	3.21	0.293	0.11	100.05
EA-1284	69.86	16.07	2.19	0.025	0.72	3.10	4.50	3.07	0.289	0.13	99.97
EA-984A	70.53	15.66	1.64	0.016	0.57	2.81	4.30	4.06	0.286	0.10	99.99
EA-984B	71.47	15.04	1.54	0.012	0.61	2.74	3.89	4.34	0.260	0.09	100.01
EA-901	70.25	16.03	1.97	0.013	0.68	2.93	4.66	3.10	0.275	0.10	99.99
Leucogranite											
EA-447	78.38	11.82	0.67	0.010	0.22	0.55	2.71	5.49	0.134	0.02	100.00
EA-577	77.07	12.39	0.95	0.008	0.33	0.61	2.70	5.74	0.182	0.03	100.01

The Sr and Nd data obtained here are similar to those obtained by Haschke (2002) for the Pajonal–El Abra complex (Fig. 12a), and the restricted variation range has not correlation either with age or SiO$_2$ content (Tables 2, 3). Lead isotopes are similar to the Andean Southern Volcanic Zone (SVZ) (Fig. 12b). The Sr isotope has not a significant tendency regarding with Sr content (Fig. 12c).

Mineral chemistry

To evaluate the variation of amphibole, apatite, and sphene modal abundances on whole rock chemistry, the concentration of REE, Sr, and Y was analyzed in these mineral phases. Minerals from Antena granodiorite (~38 Ma), which is equivalent to Clara granodiorite, were used. Trace

Fig. 8 **a** Na_2O+K_2O vs. SiO_2 wt% diagram. The *solid line* is after Irvine and Baragar (1971). **b** TAS classification diagram (Le Bas et al. 1986). *Dotted line* after Irvine and Baragar (1971). **c** AFM classification diagram (Irvine and Baragar 1971). **d** Aluminum saturation index (ASI) classification diagram
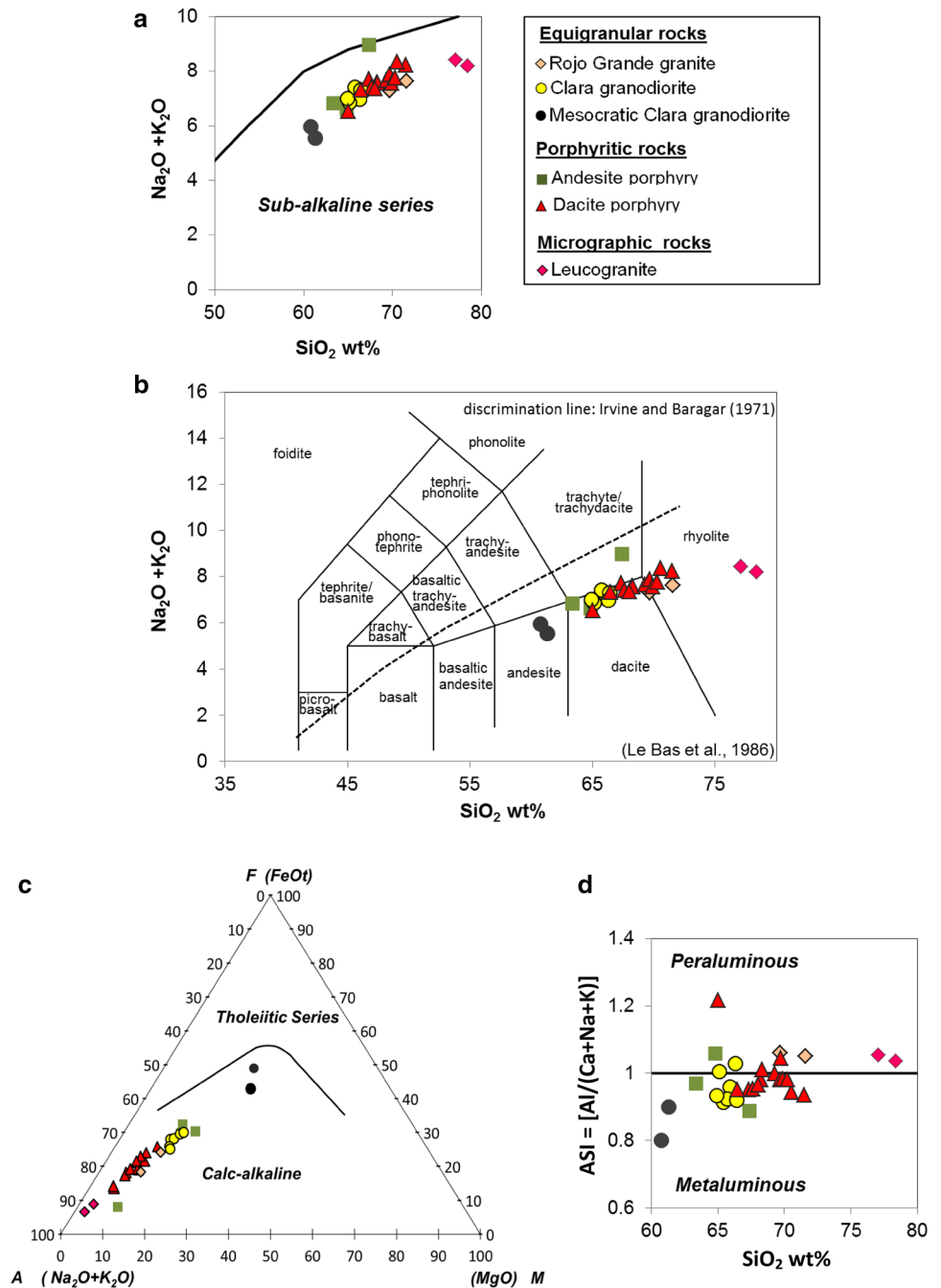

element compositions are listed in Table 4. As expected, REE contents are one order of magnitude higher in sphene than in apatite, and in turn, REE in apatite are about four times higher than in amphibole. These three minerals are also the major REE-hosts in the coeval Fiesta granodiorite and San Lorenzo porphyry from the same batholith (Rabbia et al. 2012), which is certainly valid for most arc-related felsic rocks elsewhere (e.g., Henderson 2013).

The mesocratic Clara granodiorite, which is coetaneous to Clara granodiorite, but does not display an adakitic signature (Fig. 10), tends to present a high modal abundance of amphibole, apatite and sphene (online resource ESM_2). The mesocratic Clara granodiorite (EA-1116) plots along a theoretical mixing line between Clara granodiorite (sample EA-860) and an amphibole-rich aggregate (Hb_{86} Ap_9 Sph_5) as shown in Fig. 13a and b. The addition of amphibole plus REE-rich accessory minerals to a typical Clara granodiorite sample reproduce the Sr/Y, La/Yb, and Eu/Eu* ratios of the mesocratic Clara granodiorite (EA-1116).

Fig. 9 Harker diagrams major elements vs. SiO$_2$. The older, premineral equigranular rocks are plotted along with the younger intra-mineral porphyritic rocks. Although they roughly defining variation trend, note that younger Andesite porphyry samples are less evolved than the older Rojo Grande granite. Note also that in most graphics the Mesocratic Clara granodiorite samples do not plot along the trends
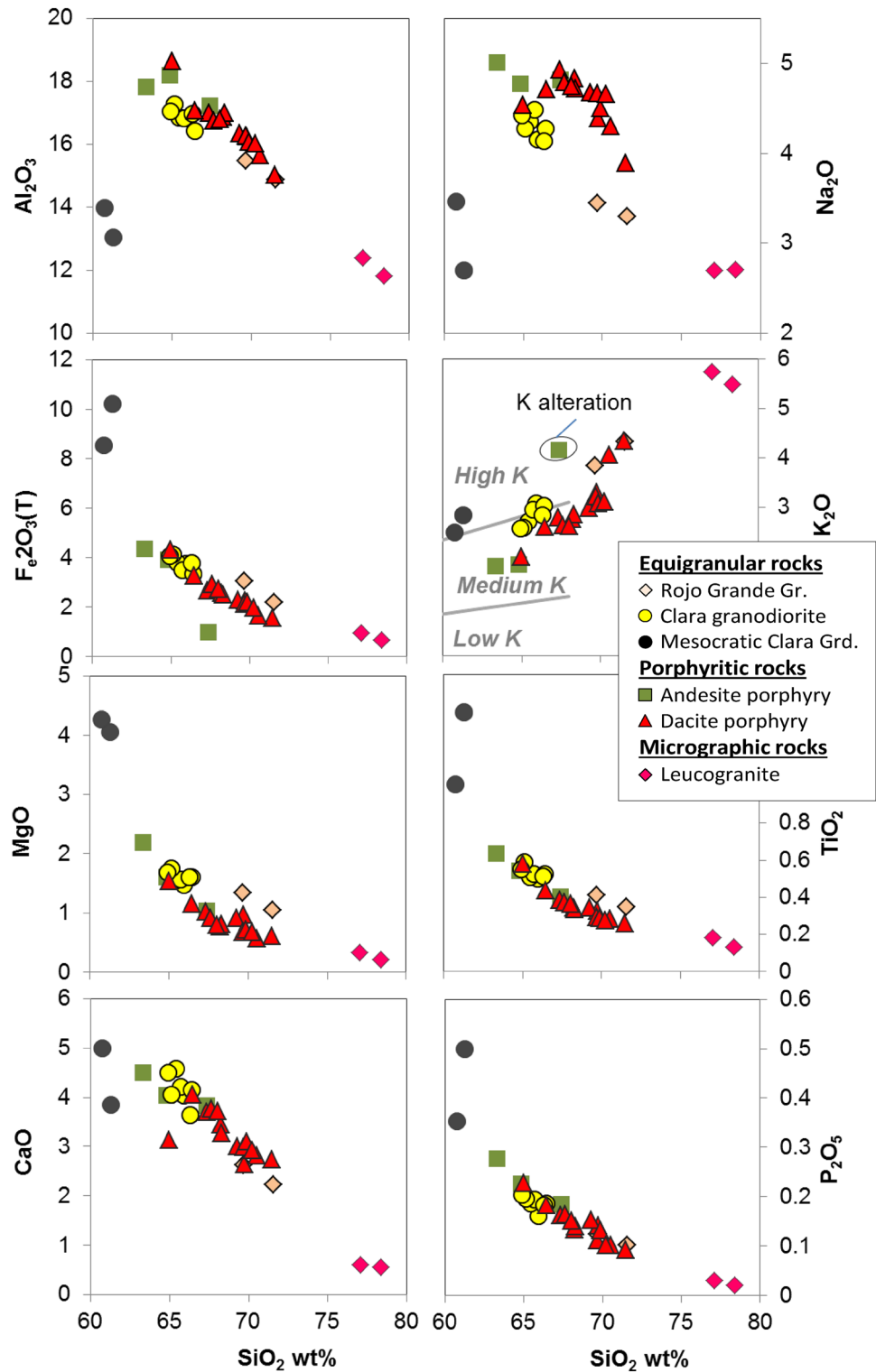

Discussion

Based on available geochemical data (Ballard 2001; Ballard et al. 2002; Haschke 2002; Rojas 2015) and Table 2 and online resource (ESM_4) of this work, the ~8.6 Ma-long

magmatic history of the El Abra deposit, extending from ~45 to 36 Ma (Correa et al. 2016) can be divided in two distinct stages: (a) An older stage (>38.7 Ma) represented by rocks having a "normal" (non-adakite) arc geochemistry; and (b) A younger stage (<38.7 Ma) characterized by

Fig. 10 Trace element diagrams showing compositional fields of adakites and arc andesite–dacite–rhyolite (ADR) fields defined by Castillo et al. (1999). Symbols as in Fig. 9
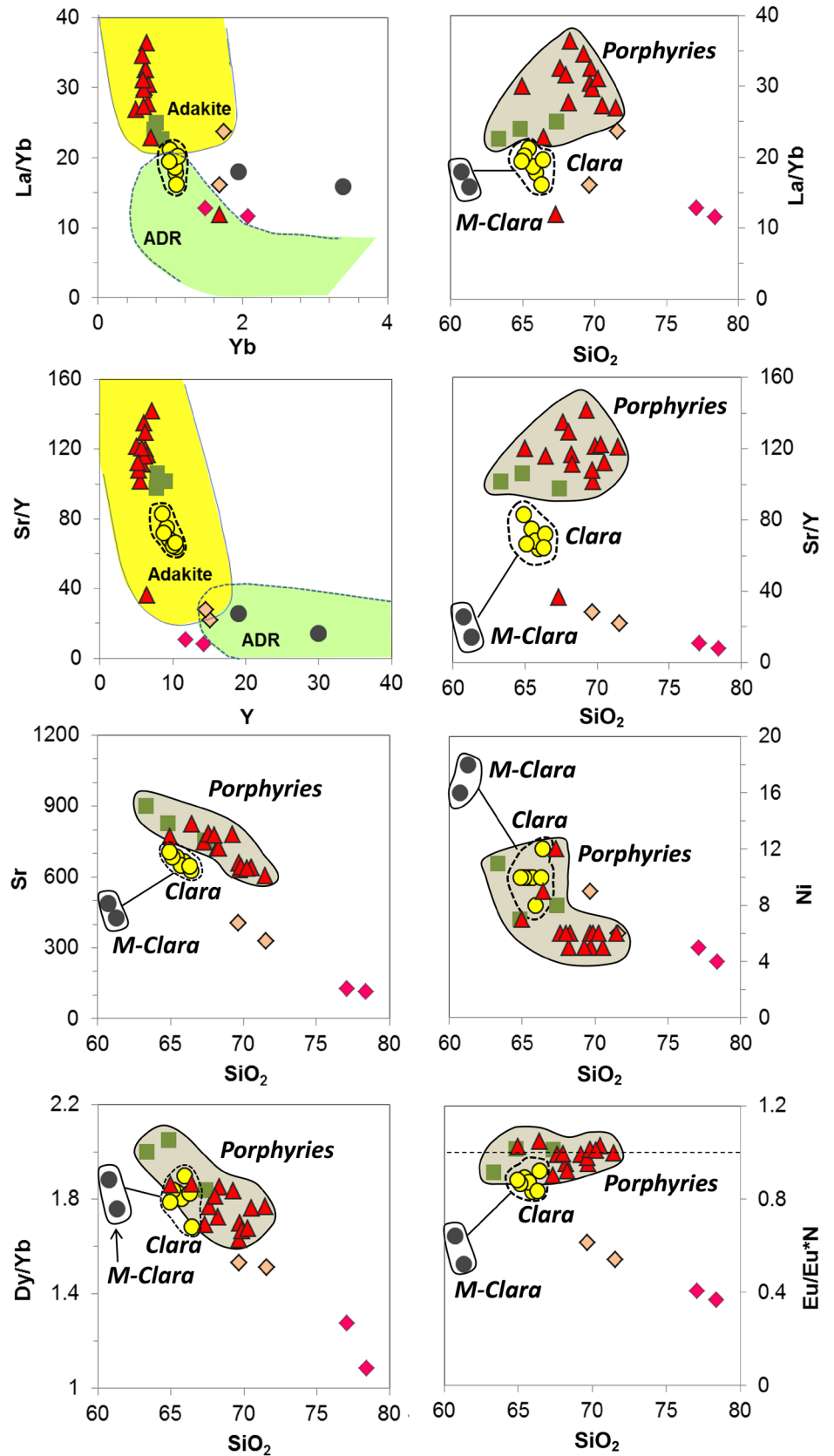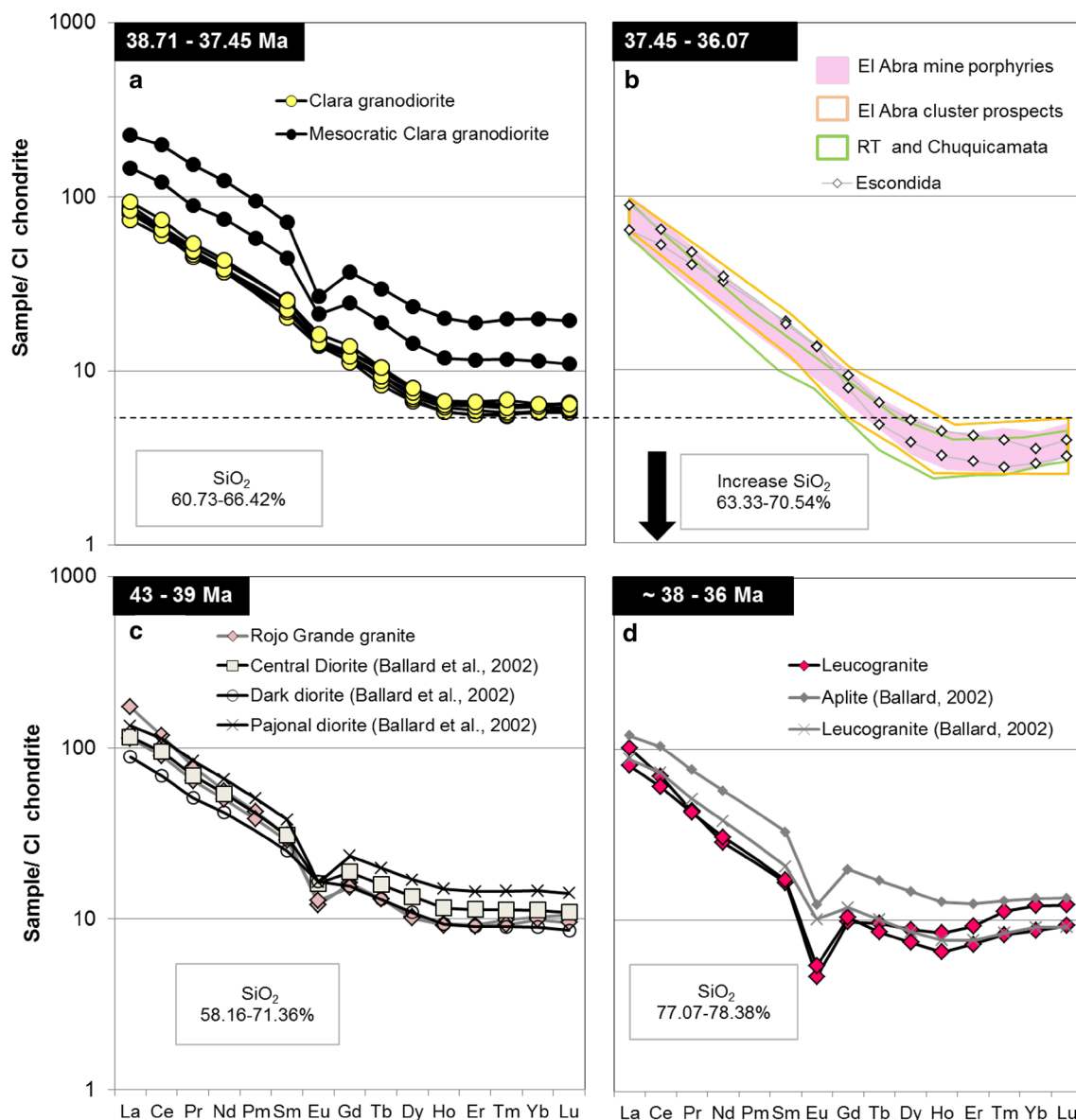
Fig. 11 REE diagrams. **a** Clara granodiorite and mesocratic Clara granodiorite. **b** Intramineral porphyries from The El Abra and Chuquicamata districts. **c** Equigranular premineral rocks. **d** Filter pressed segregated melts. Data from: Cabrera et al. (2010); Rojas (2015); Ballard et al. (2002); Richards et al. (2001). Normalized values to CI-chondrite Sun and McDonough (1989). Promethium (Pm), if plotted, is interpolated between Nd and Sm

a suite of rocks having an adakite-like arc geochemistry (Fig. 14a–c).

The age-constrained geochemical data compiled in Fig. 14a–c show that some rock units do not display the adakite-like signature despite being younger than 38.7 Ma; this includes the most mafic rocks (e.g., the mesocratic Clara granodiorite) and some of the most felsic ones (e.g., the Apolo granite and aplites and the leucogranites).

A closer analysis, however, suggests that the extreme evolved character (e.g., ~70–78 wt% of SiO_2) of the more felsic units is the reason for the apparent lack of an adakite-like geochemical signature. The very low Al_2O_3, CaO and Sr contents (down to ~11.8 wt%; 0.55 wt% and 115 ppm, respectively, Table 2 and online resource ESM_4), the strong depletion in REE's with variable, but mostly negative Eu anomaly (Fig. 15), and the higher $^{87}Sr/^{86}Sr$ ratios (Fig. 12c) of these rocks suggest that their parental melts fractionated plagioclase (e.g., AFC-process). Besides, some of these silicic rocks have been previously interpreted as segregated or filter-pressed melts (Ballard et al. 2002). Although we cannot completely rule out potential alteration effects (e.g., some Sr or Eu

Table 3 Sr, Nd, and Pd isotope data

Rock unit	Rojo Grande granite	Clara granodiorite	Mesoc. Clara granodiorite	Abra porphyry			Leucogranite
				Dacite	Dacite	Rhyolite	
Sample	EA-657	EA-1141	EA-1116	EA-561	EA-662	EA-1284	EA-477
Coordinates							
N	16599.79	76,300	76199.97	76460.11	76000.15	76748.52	76748.52
E	76599.78	17,100	16900.15	17959.73	17399.44	17848.51	17848.51
Age[a]	39.09 ± 0.03	38.74 ± 0.10	37.45 ± 0.09	37.49 ± 0.10		36.07 ± 0.15	
$^{87}Sr/^{86}Sr$	0.705159	0.704796	0.704822	0.704681	0.704695	0.704722	0.706611
$^{87}Sr/^{86}Sr_i$	0.704578	0.704577	0.704541	0.704551	0.704571	0.704558	0.704890
$^{143}Nd/^{144}Nd$	0.512671	0.512660	0.512647	0.512654	0.512644	0.512654	0.512655
$^{143}Nd/^{144}Nd_i$	0.512642	0.512630	0.512618	0.512625	0.512620	0.512629	0.512625
$^{208}Pb/^{204}Pb$	38.60	38.60	38.80	38.52	38.63	38.56	38.95
$^{208}Pb/^{204}Pb_i$	38.15	38.22	38.08	38.31	38.46	38.43	38.32
$^{207}Pb/^{204}Pb$	15.59	15.61	15.64	15.62	15.63	15.61	15.66
$^{207}Pb/^{204}Pb_i$	15.57	15.59	15.60	15.61	15.62	15.60	15.61
$^{206}Pb/^{204}Pb$	18.94	18.77	18.86	18.71	18.70	18.70	19.31
$^{206}Pb/^{204}Pb_i$	18.46	18.36	18.09	18.49	18.54	18.52	18.30

[a] From Correa et al. (2016)

Fig. 12 a $^{87}Sr/^{86}Sr_{initial}$ vs. $^{143}Nd/^{144}Nd_{initial}$ diagram. Data from this study and Haschke (2002). **b** $^{87}Sr/^{86}Sr_{initial}$ vs. $^{207}Pb/^{204}Pb_{initial}$. **c** $^{87}Sr/^{86}Sr_{initial}$ vs. Sr
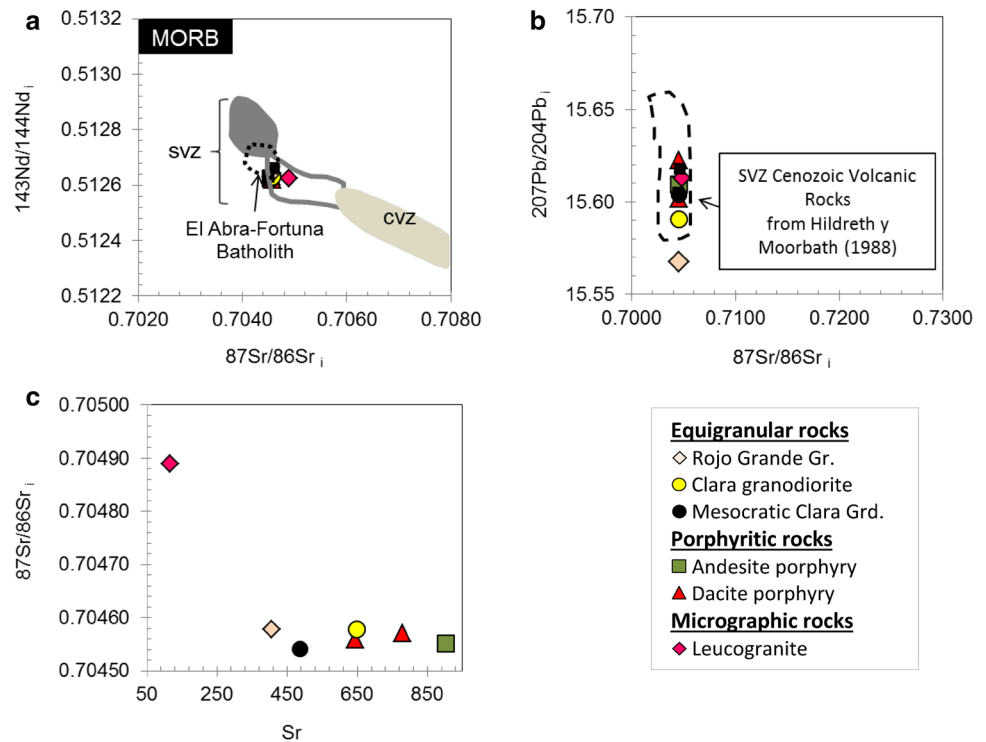
leaching), we do argue that an extended plagioclase fractionation at shallow to mid-crustal levels (i.e., AFC ± filter-pressing processes) obliterated the adakite-like features (Sr/Y >40 or La/Yb$_n$ >13–15; Fig. 14a–c) of these evolved residual melts (e.g., Apolo granite and related rocks). Notwithstanding, shallow crustal plagioclase

fractionation affected some, but not all of the high-SiO$_2$ (>70 wt%) intrusions (Fig. 14a–c). For example, the youngest sample in Fig. 14 corresponds to a rhyolite porphyry (34.30 Ma; Rojas 2015) from the El Abra district that despite the high SiO$_2$ content (70.8 wt%) retained high Al$_2$O$_3$, CaO and Sr contents (16.0 wt%; 3.5 wt% and

Table 4 Rare earth elements (REE), Sr and Y contents in sphene, apatite, and amphibole

Analysis method	LA-ICP-MS							
Analyte symbol	Sr	Y	La	Ce	Pr	Nd	Sm	Eu
Unit symbol	ppm	ppm	ppm	ppm	ppm	ppm	ppm	ppm
Sphene								
RT13sph4_1	18.9	501	993.6	3284.1	424.5	1543.0	226.7	51.0
RT13sph4_2	19.0	394	974.4	3051.3	380.1	1332.2	178.2	50.1
RT13sph4_3	19.7	343	937.8	2827.6	336.5	1163.3	155.5	49.9
RT13sph4_4	18.8	424	856.8	2818.3	361.5	1322.9	189.2	46.8
RT13sph4_5	21.2	1043	2382.3	8739.6	810.9	2818.1	407.0	122.5
RT13sph8_1	19.4	980	388.8	1852.1	318.4	1461.7	298.1	59.4
RT13sph8_2	22.6	1021	429.3	2233.7	361.6	1611.1	321.7	73.9
Apatite								
RT13ap9	233.5	62.6	594.4	866.8	80.9	299.3	41.2	6.8
RT13ap7_1	216.5	55.0	415.4	706.6	62.9	209.0	26.2	3.7
RT13ap7_2	221.6	63.4	441.4	689.2	63.5	218.6	27.9	4.1
RT13ap7_3	219.0	61.5	397.6	640.1	59.0	214.0	30.7	3.8
Amphibole								
RT13hbl14_1	10.0	269.4	31.82	153.7	29.2	151.1	46.9	1.5
RT13hbl14_2	10.9	330.5	39.10	185.6	35.9	179.9	57.2	1.7
RT13hbl14_3	13.1	272.5	35.52	173.4	33.0	172.4	53.6	1.9
Analysis method	LA-ICP-MS							
Analyte symbol	Gd	Tb	Dy	Ho	Er	Tm	Yb	Lu
Unit symbol	ppm	ppm	ppm	ppm	ppm	ppm	ppm	ppm
Sphene								
RT13sph4_1	148.6	18.1	92.0	17.2	49.2	6.8	50.3	7.7
RT13sph4_2	111.5	14.0	72.8	13.5	38.9	5.4	43.9	6.7
RT13sph4_3	97.0	12.0	61.2	11.7	32.5	4.5	34.6	5.7
RT13sph4_4	115.7	14.3	74.6	14.3	38.9	5.9	40.6	6.1
RT13sph4_5	268.7	33.6	181.0	36.0	100.6	15.5	115.2	18.6
RT13sph8_1	233.1	33.0	181.3	33.9	95.7	13.7	93.6	13.7
RT13sph8_2	247.3	34.1	187.1	35.1	94.6	14.2	97.7	14.6
Apatite								
RT13ap9	35.5	3.4	13.9	2.5	4.8	0.5	3.0	0.4
RT13ap7_1	20.0	2.2	10.0	1.8	4.7	0.5	3.3	0.6
RT13ap7_2	23.7	2.4	11.1	2.2	5.4	0.7	4.3	0.6
RT13ap7_3	25.4	2.5	13.1	2.3	4.7	0.5	3.6	0.7
Amphibole								
RT13hbl14_1	43.2	7.4	43.3	9.6	27.7	4.3	30.1	4.3
RT13hbl14_2	55.4	9.1	57.1	11.3	33.6	4.9	37.7	5.3
RT13hbl14_3	50.5	8.0	50.6	9.6	27.8	4.1	30.5	4.1

589 ppm, respectively; Rojas 2015), resulting in an adakite-like signature (e.g., Sr/Y 125.3; La/Yb$_n$ 27.3; Rojas 2015). This suggests that some of the young (<38.7 Ma) silicic rocks, such as the rhyolite porphyry, have evolved mostly at high-pressure (see below), without significant plagioclase fractionation at shallow crustal levels.

In the case of the mesocratic Clara granodiorite, local variations in modal mineralogy (e.g., increase in amphibole, apatite and sphene, including rutile after sphene-, online resource ESM_2), may account for the apparent inconsistency in the geochemistry-age relationship (Fig. 14). Figure 13a, b show that the mesocratic Clara
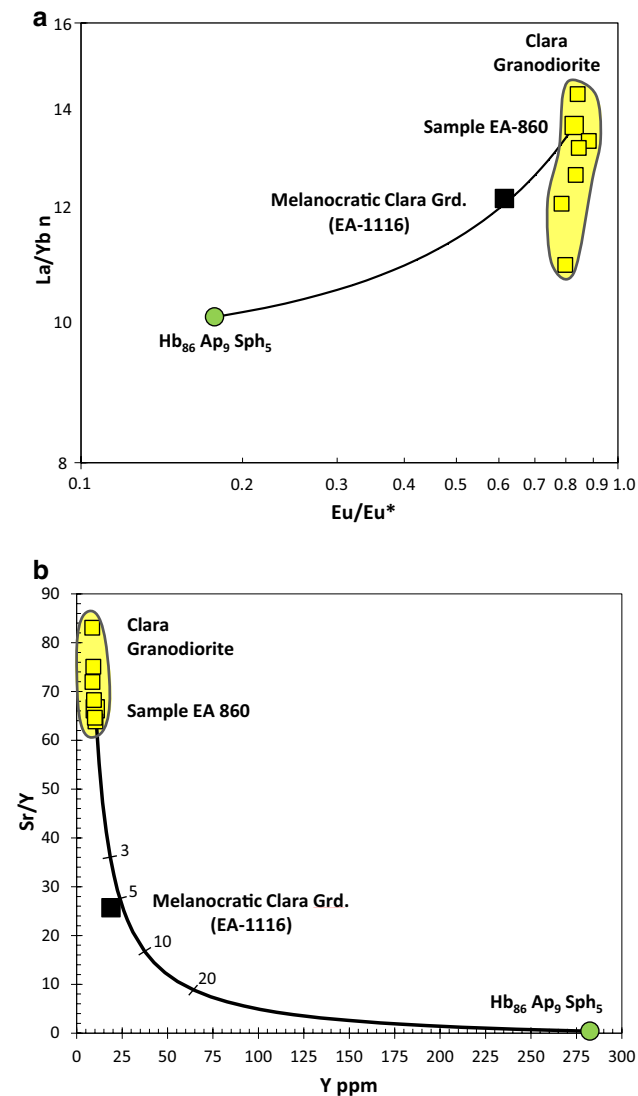
Fig. 13 **a** La/Yb$_n$ vs. Eu/Eu* diagram showing the theoretical mixing line between the Clara granodiorite (simple EA-860) and an amphibole-rich composite (Hb$_{86}$ Ap$_9$ Sph$_5$). All data are chondrite normalized. **b** Sr/Y vs. Y diagram showing the theoretical mixing line between the Clara granodiorite (simple EA-860) and an amphibole-rich aggregate (Hb$_{86}$ Ap$_9$ Sph$_5$). In both cases the Melanocratic Clara granodiorite (sample EA-1116) plots along this mixing line. *Marks* and *numbers on the mixing line* represent the mixing percentage of the amphibole-rich aggregate

granodiorite (sample EA-1116) plots along a theoretical mixing line between a typical Clara granodiorite (sample EA-860) and a hypothetical amphibole-rich cumulate (amphibole-apatite-sphene in 86:9:5 proportions). This simple mixing model closely reproduces the Sr/Y, La/Yb, and Eu/Eu* ratios of the mesocratic Clara granodiorite, and may explain why the geochemistry of these amphibole-rich rocks departs from an adakite-like composition. The origin of the high modal abundances of amphibole and REE-bearing accessory phases in the mesocratic granodiorites is

less clear and more complex to determine. The coarse grain size of these rocks precludes them from being synplutonic "chilled" mafic dikes or enclaves. These thin (<0.5 m) bands of the mesocratic rocks, inside the volumetrically dominant Clara granodiorite, possibly represent local melt pockets. Alternatively, they may represent a cumulate rich in early-crystallized megacrystic amphibole and accessory phases. In this sense, the resulting composition of the amphibole-rich layers may significantly differ from melt composition. In any case, the localized high modal abundance of amphibole, along with the large size (up to 20 mm) and euhedral shape of amphibole crystals (Fig. 4g) of these mafic granodiorites, suggests a high-water activity in the related silicate melt. Unfortunately, further discussion on the real extension, shape and nature of these mesocratic granodiorites is hindered by the absence of outcrops and the limited size of the samples recovered from deep drillcores. Nevertheless, the intimate coexistence of amphibole-rich (non-adakite) with adakite-like rocks, offers an explicit clue for the role of amphibole in the petrogenesis of these granodiorite rocks. The adakite-like geochemistry, with Sr/Y >60 (online resource ESM_4) indicates that the volumetrically dominant Clara granodiorite (and mesocratic lenses) is associated with parental melt evolution without significant plagioclase fractionation at low-pressure conditions (e.g., <0.4 GPa), where plagioclase may crystallize before amphibole (Grove et al. 2003). Besides, the Sm/Dy ratios of these rocks suggest that their parental melt may have evolved at deep crustal levels, because the Sm/Dy ratios in igneous arc rocks increases in response to amphibole (±garnet) fractionation (Schütte et al. 2011 and references there in). It is evident from Fig. 16 that the presence of amphibole (±garnet) in the evolution of younger magmas (<38.7 Ma), including the Clara granodiorite, was more important than in the older non-adakite ones. This implies that the adakite-like rocks evolved at deep-crustal conditions and from H$_2$O-rich magmas, where amphibole (±garnet) is expected to be a dominant early phase (e.g., Alonso-Perez et al. 2009).

Although there is a general agreement on the role of amphibole (±garnet) fractionation in developing the adakite-like signature of magmas associated with porphyry copper deposits, its role is commonly regarded as "cryptic" (Rohrlach and Loucks 2005; Schütte et al. 2011; Richards 2011; Rooney et al. 2011; Chiaradia et al. 2012). The intimate coexistence of amphibole-rich rocks (mesocratic Clara granodiorite) with adakite-like rocks (Clara granodiorite) at the El Abra deposit, offers a more tangible evidence supporting the amphibole (and REE-rich accessory phases) fractionation as a driving process in developing the adakite-like feature in felsic magmas associated with ore deposits. Besides, the comparable Nd–Sr–Pb isotope ratios of non-adakite and adakite-like rocks (Table 3; Fig. 12)

suggest similar magma sources for these contrasting rock
suites. Therefore, the geochemical features that character-
ize these two groups of rocks may result from the different
crustal conditions under which they have evolved.

When the El Abra magmatic evolution is linked to the
Andean geotectonic context, it becomes clearer what
the causes are that may have triggered the appearance of
the adakite-like geochemical signature in the younger
(<38.7 Ma) intrusions. By mid-Eocene times, prior to the
formation of the El Abra porphyry copper deposit, the rela-
tively fast convergence rate between the Nazca and South
American plates (Fig. 17) could have favored higher melt
production in the underlying asthenospheric mantle wedge
as well as higher compressional stress in the overriding
upper plate (Bertrand et al. 2014). By late Eocene times,
this compressional tectonic regime, the Incaic orogeny,
resulted into crustal thickening beyond 45 km as a conse-
quence of increased horizontal shortening of the arc crust
(Mpodozis and Cornejo 2012). Consequently, magmas
trapped at deep crustal levels were forced to evolve under
high pressure conditions. The timing at which the period of
fast convergence rate ended (~38–39 Ma, Fig. 17) coincides
with the appearance of the adakite-like signature in rocks
from El Abra (~38.7 Ma; Fig. 14), indicating that kinemati-
cally-induced arc-relaxation may have favored ascension of
fertile magmas, from the deeper "hot zone" to middle and
upper crustal levels. This geodynamic context has already
been proposed for large-scale porphyry copper distribution
in the Andes (Bertrand et al. 2014 and references therein).

Temporal evolution of the adakite-like magmas

When the ~2 Ma evolution period between the intrusion of
the Clara granodiorite and the younger El Abra porphyries
is considered, it becomes evident that the adakite charac-
ter of the intrusions increases over time. This can be noted
in the progressive increase of the Sr/Y and Sm/Dy ratios
(Figs. 14a, 16) along with the growing depletion of MREE
and HREE's (Figs. 10, 11) and a decrease in Dy/Yb$_n$ ratios
(not shown). These geochemical changes are consistent
with a systematic increase in amphibole fractionation at
depth, which in turn implies an evolution towards more
hydrated (and oxidized?) magmas. Independent evidence
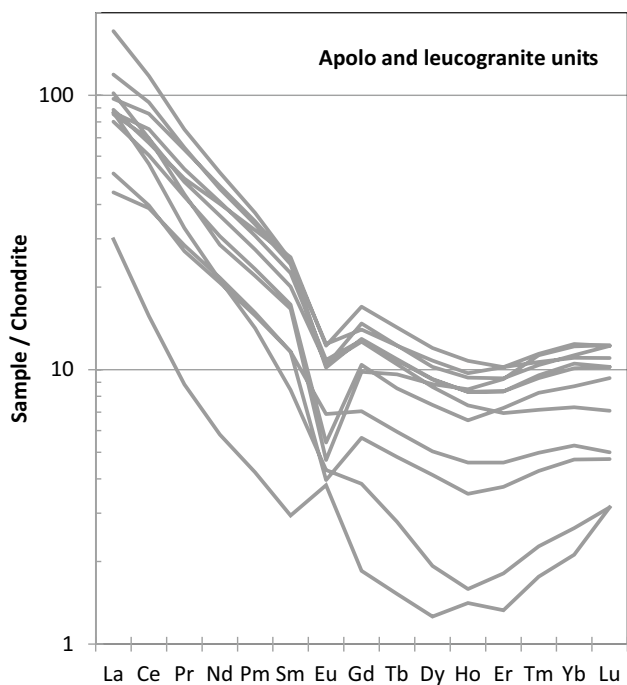from zircon Ce$^{(IV)}$/Ce$^{(III)}$ and Eu/Eu* ratios support higher
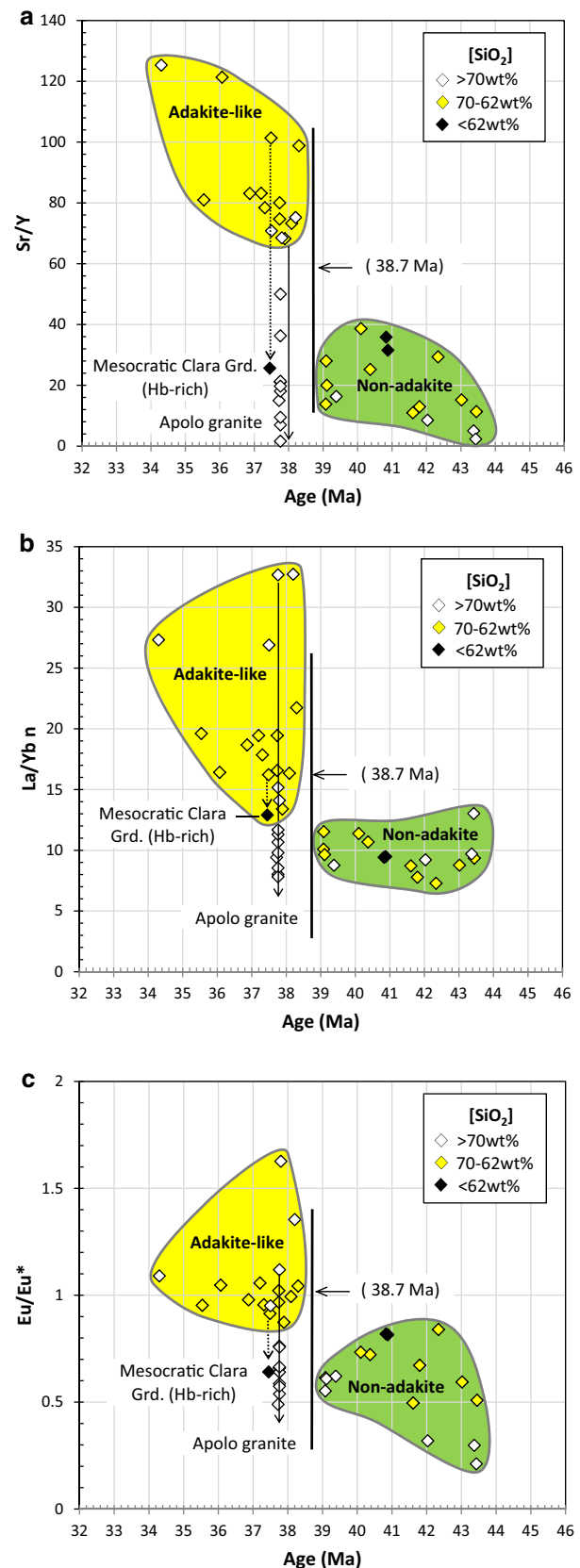
Fig. 15 Chondrite normalized REE patterns for Apolo granites and aplites from Ballard (2001), Ballard et al. (2002), Rojas (2015) and leucogranites from this work
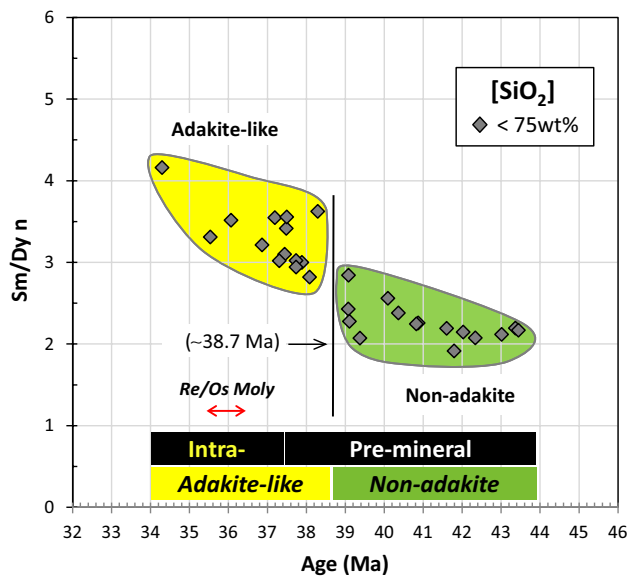

Fig. 16 Chondrite normalized Sm/Dy ratio vs. U-Pb zircon age diagram for samples with less than 75 wt% of SiO_2 contents. Published data from Ballard (2001); Ballard et al. (2002); Haschke (2002); Rojas (2015) and Correa et al. (2016) are included to complement those presented here. The Sm/Dy$_n$ ratios are higher in the younger (<38.7 Ma) group of rocks, highlighting the presence of amphibole (±garnet) in their petrogenesis. The *red arrow* represents molybdenite Re/Os ages of the mineralization in the El Abra district after Correa et al. (2016). Intra- and premineral stand for porphyry rocks associated with mineralization and equigranular rocks older than mineralization, respectively
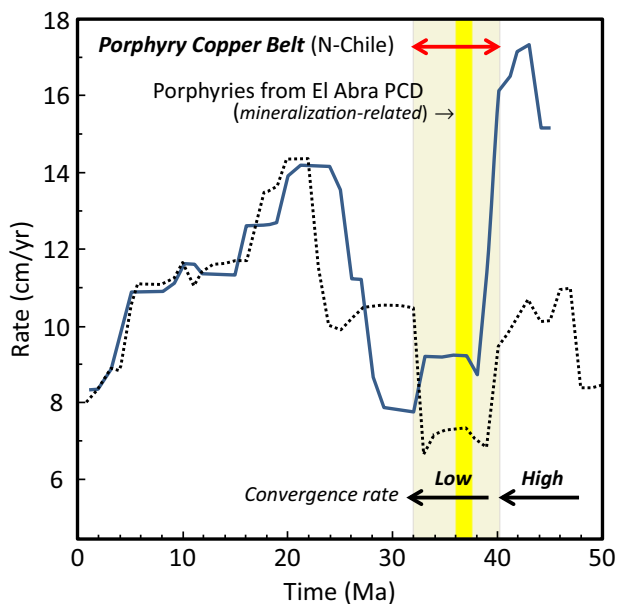

Fig. 17 Rates of convergence (cm/year) vs. time (Ma) of the Nazca (Farellones) plate relative to fixed South America, showing the kinematic context in which the El Abra porphyry copper deposit was emplaced (*light gray* band) along the Andean margin. *Blue line* Nazca (Farellones) plate (20°S/72°W), UTIG PLATES model and dotted line Nazca (Farellones) plate (20°S/72°W), EarthByte model (modified after Bertrand et al. 2014). *Black arrows* indicate periods of high and low convergence rates of plates. *Red arrow* encompasses the age (late-Eocene to early-Oligocene) of the porphyry copper belt from northern Chile to which the El Abra deposit belongs

magmatic oxidation states in the younger and felsic intrusive units of the El Abra porphyries (Ballard et al. 2002).

This interpretation of the magmatic evolution coincides with the progressive building of a large, long-lived magmatic reservoir at depth, as proposed by Correa et al. (2016), based on the "subtle inheritance" of zircons detected in the El Abra porphyries. Additional evidence for the reworking of earlier intrusions is preserved in microtextures such as core dissolution, patchy and sieve textures, as well as compositional variations (e.g., increase of An, Sr and Fe contents towards the rims) of plagioclase phenocrysts from the El Abra porphyry. These plagioclase features have been interpreted as the result of repeated hot magma input, providing additional heat for assimilation of earlier intrusions (e.g., Pietranik et al. 2006; Renjith 2014). The input of a less-evolved magma to the El Abra magmatic system may also be derived from the lower SiO_2 and higher MgO contents of some samples from the El Abra porphyry (e.g., EA-561 with 63.3 and 2.19 wt%, respectively; Table 2) compared to the slightly older and more abundant Clara granodiorite (64.9–66.4 wt% SiO_2 and 1.47–1.75 wt% MgO; Table 2). This suggests the arrival of hotter, less-evolved and deep-sourced magma into the mid-to-upper crustal levels, shortly before the El Abra porphyry

dikes were intruded. These porphyries, which crystallized from a hydrous and oxidized magma, are associated with the main mineralization event (36.25 ± 0.25 Ma) at El Abra deposit (Correa et al. 2016).

Concluding remarks

At the El Abra porphyry copper deposit two contrasting rock suites are recognized: (a) an older suite (>38.7 Ma), composed by intrusive rocks with "normal" (non-adakite) arc geochemistry and (b) a younger one (<38.7 Ma), represented by intrusive rocks with adakite-like arc geochemistry. The evolution over time from non-adakite to adakite-like magmatism at El Abra district coincides with the development of a compressive (and/or transpressive) tectonic regime, the Incaic orogeny, as a consequence of a period of fast convergence between the Farellones and South American plates. This tectonic event led to the shortening and thickening of the arc crust forcing the lower crust to evolve under higher pressure conditions, where amphibole ($\pm$garnet$\pm$REE-bearing accessory phases) fractionates (as cumulates and/or or restite) in the absence of plagioclase. This has driven the residual melt towards adakite-like compositions, with higher Sr/Y and La/Yb ratios and Al- and Na-rich contents (e.g., Rapp and Watson 1995; Petford and Gallagher 2001; Rohrlach and Loucks 2005; Richards 2011). Besides, the compressional episode likely induced a slowdown of magma ascent rate through the crust, increasing the residence time and favoring extensive differentiation leading to water-rich, oxidized felsic melts where amphibole became a prominent crystal fractionate (e.g., Richards et al. 2001; Richards and Kerrich 2007; Chiaradia et al. 2009; Chiaradia 2014; Loucks 2014). The compressional regime also contributed to the building of long-lived, mid- to upper-crustal magmatic reservoirs from where magma episodically escaped, at least for a 1.4 Ma time period (Correa et al. 2016), to form the porphyritic apophyses associated with copper mineralization at the El Abra deposit.

Extensive low-pressure (<0.4 GPa) fractionation of plagioclase (AFC$\pm$filter-pressing processes) may have minimized or obliterated the adakite-like feature of some evolved rocks, such as the Apolo granite and aplites and the leucogranites. Finally, the amphibole-rich lenses of the (non-adakite) mesocratic Clara granodiorite hosted by the (adakite-like) Clara granodiorite represent a concrete evidence of the amphibole role in the development of the adakite signature associated with a porphyry copper deposit.

References

Alonso-Perez R, Müntener O, Ulmer P (2009) Igneous garnet and amphibole fractionation in the roots of island arcs: experimental constraints on andesitic liquids. Contrib Mineral Petrol 157:541

Ardila R (2009) Eventos de mineralización de sulfuros en la Mina El Abra, Internal report from Sociedad Contractual Minera El Abra SCMEA, p 54

Ballard JR (2001) A comparative study between the geochemistry of ore-bearing and barren calc-alkaline intrusions. Unpublished PhD. thesis, The Australian National University, Canberra, p 254

Ballard JR, Palin M, Campbell I (2002) Relative oxidation states of magmas inferred from CeIV/CeIII in zircon: application to porphyry copper deposits of northern Chile. Contrib Mineral Petrol 144:347–364

Barrett LF (2004) Geology and status of exploration projects, El Abra District, II Region, Chile. Internal SCMEA report, El Abra. p 6–37

Bertrand G, Guillou-Frottier l, Loiselet C (2014) Distribution of porphyry copper deposits along the western Tethyan and Andean subduction zones: Insights from a paleotectonic approach. Ore Geol Rev 60:174–190

Cabrera JM, Rabbia OM, Parra A (2010) Caracterización Petrológica de la Fuente Magmática del Depósito Radomiro Tomic. CODELCO Norte Biennial Conference of Geosciences. Calama, p 1–14

Campbell IH, Ballard JR, Palin JM, Allen C, Faunes A (2006) U–Pb zircon geochronology of granitic rocks from the Chuquicamata-El Abra Porphyry Copper Belt of Northern Chile: Excimer Laser Ablation ICP-MS Analysis. Econ Geol 101:1327–1344

Castillo P, Janney P, Solidum R (1999) Petrology and geochemistry of Camiguin Island, southern Philippines: insights to the source of adakites and other lavas in a complex arc setting. Contrib Mineral Petrol 134:33–51

Chelle-Michou C, Chiaradia M, Béguelin P, Ulianov A (2015) Petrological evolution of the magmatic suite associated with the Coroccohuayco Cu(–Au–Fe) Porphyry-Skarn Deposit, Peru. J Petrol 56:1829–1862

Chiaradia M (2014) Copper enrichment in arc magmas controlled by overriding plate thickness. Nat Geosci 7: 43–46

Chiaradia M, Merino D, Spikings R (2009) Rapid transition to long-lived deep crustal magmatic maturation and the formation of giant porphyry-related mineralization Yanacocha, Peru. Earth Planet Sci Lett 288:505–515

Chiaradia M, Ulianov A, Kouzmanov K, Beate B (2012) Why large porphyry Cu deposits like high Sr/Y magmas? Nature 685:1–7

Cornejo P, Mpodozis C, Mora R (2014) Geologic map of the Collahuasi-Calama belt. Antofagasta Minerals, SA

Correa K, Rabbia O, Hernandez L, Selby D, Astengo M (2016) The timing of magmatism and ore formation in the El Abra porphyry copper deposit, northern Chile: Implications for long-lived multiple-event magmatic-hydrothermal porphyry systems. Econ Geol 111:1–28

Dilles JH, Tomlinson A, Marti MW, Blanco N (1997). El abra and fortuna compleexes: a porphyry copper batholith sinistrally

displaced by the falla oeste. VIII Congreso Geológico Chileno Actas, vol III:1883–1887

Dilles J, Tomlinson A, García M, Alcota H (2011) The geology of the Fortuna Granodiorite Complex, Chuquicamata district, northern Chile: Relation to porphyry copper deposits. SGA Biennial Meeting, 11th, Antofagasta, Proceedings 399–401

Dreher ST, Macpherson CG, Pearson DG, Davidson JP (2005) Re–Os isotope studies of Mindanao adakites: Implications for sources of metals and melts. Geology 33:957–960

Grove TL, Elkins-Tanton LT, Parman SW et al (2003) Fractional crystallization and mantle-melting controls on calc-alkaline differentiation trends. Contrib Mineral Petrol 145:515–533

Haschke MR (2002) Evolutionary geochemical patterns of Late Cretaceous to Eocene arc magmatic rocks in North Chile: implications for Archean crustal growth. EGU Stephan Mueller Special Publication Series 2 207–218

Hedenquist JW, Lowenstern JB (1994) The role of magmas in the formation of hydrothermal ore deposits. Nature 370:519–527

Hellstrom J, Paton C, Woodhead JD, Hergt JM (2008) Iolite: software for spatially resolved LA-(quad and MC) ICPMS analysis. In: Laser ablation ICP–MS in the earth sciences: current practices and outstanding issues. In: Sylvester P (ed) Mineral Assoc of Canada Short Course series 40:343–348

Henderson P (2013) Developments in geochemistry, volume 2: rare earth element geochemistry presents the remarkable developments in the chemistry and geochemistry of the rare earth elements. Elsevier, Amsterdam, p 510 **(ISBN 9781483289779)**

Irvine TN, Baragar WRA (1971) A guide to the chemical classification of the common volcanic rocks. Can J Earth Sci 8:523–548

Jochum KP, Stoll B, Herwig K, et al (2006) MPI-DING reference glasses for in situ microanalysis: new reference values for element concentrations and isotope ratios. Geochem Geophys Geosyst 7(2):Q02008

Kay SM, Mpodozis C (2001) Central Andean ore deposits linked to evolving shallow subduction systems and thickening crust. GSA Today 11:4–9

Kay SM, Mpodozis C (2002) Magmatism as a probe to the Neogene shallowing of the Nazca plate beneath the modern Chilean flat-slab. J South Am Earth Sci 15:39–57

Kay S, Mpodozis C, Ramos VA, Munizaga F (1991) Magma source variations for mid-Tertiary magmatic rocks associated with a shallowing subduction zone and a thickening crust in the Central Andes (28–33S). In: Harmon RS, Rapela CW (eds) Andean magmatism and its tectonic setting, Boulder, Colorado. Spec Pap Geol Soc Am 265:113–137

Kurtz AC, Kay SM, Charrier R, Farrar E (1997) Geochronology of Miocene plutons and exhumation history of the El Teniente region, Central Chile (34°-35°S). Rev Geol Chile 24(1):75–90

Le Bas MJ, Le Maitre RW, Streckeisen A, Zanettin B (1986) A chemical classification of volcanic rocks based on the total alkali-Silica diagram. J Petrol 27:745–750

Loucks RR (2014) Distinctive composition of copper-ore-forming arc magmas. Aust J Earth Sci 61:5–16

Maksaev V, Zentilli M (1999) Fission track thermocornology of the Domeyko Cordillera, Northern Chile: implications for Andean tectonics and porphyry copper metallogenesis. Explor Min Geol 8:65–89

Mpodozis C, Cornejo P (2012) Cenozoic tectonics and porphyry copper systems of the Chilean Andes. Soc Eco Geo Spc Pub 16:329–360

Mpodozis C, Marinovic N, Smoje I, Coutiño L (1993) Estudio geológico estructural de la cordillera de Domeyko entre Sierra Limón Verde y Sierra Mariposas, región de Antofagasta: Servicio Nacional de Geología y Minería – Corporación Nacional del Cobre (Chile), Informe registrado IR-93-04, p 282

Oyarzun R, Márquez A, Lillo J, López I, Rivera S (2001) Giant versus small porphyry copper deposits of Cenozoic age in northern Chile: adakite versus normal calc-alkaline magmatism. Miner Depos 36:794–798

Perelló J, Carlotto V, Zárate A, Ramos P, Posso H, Neyra C, Caballero A, Fuster N, Muhr R (2003) Porphyry-style alteration and mineralization of the middle Eocene to early Oligocene Andahuaylas-Yauri belt, Cuzco region, Peru. Econ Geol 98:1575–1605

Petford N, Gallagher K (2001) Partial melting of mafic (amphibolitic) lower crust by periodic influx of basaltic magma. Earth Planet Sci Lett 193:483–499

Pettke T, Oberli F, Heinrich CA (2010) The magma and metal source of giant porphyry-type ore deposits, based on lead isotope microanalysis of individual fluid inclusions. Earth Planet Sci Lett 296:267–277

Pietranik A, Koepke J, Puziewicza J (2006) Crystallization and resorption in plutonic plagioclase: implications on the evolution of granodiorite magma Gęsiniec granodiorite, Strzelin Crystalline Massif, SW Poland. Lithos 86:260–280

Rabbia OM. Hernández LB (2000) Quartz diorite trend in porphyry copper deposits: underlying petrological processes and implications in copper metalogenesis. Miner Metalog 6:416–423

Rabbia OM, Hernández LB, King RW, López-Escobar L (2002) Discusión on "Giant versus small porphyry copper deposits of Cenozoic age in northern Chile: adakite versus normal calc-alkaline magmatism" by Oyarzun et al. (Miner Depos 36:794–798, 2001). Miner Depos 37:791–794

Rabbia OM, Hernandez LB, Cabrera JM, Ulrich T, Bissig T, Parra A (2012) Evidencias de movilidad de las REE en depósitos tipo pórfido de cobre durante la alteración hidrotermal. Congreso Geológico Chileno, 13, Antofagasta, Chile, 5–9 Agosto 2012:90–92

Rapp RP, Watson EB (1995) Dehydration melting of metabasalt at 8–32 kbar: implications for continental growth and crust–mantle recycling. J Petrol 36:891–931

Renjith ML (2014) Micro-textures in plagioclase from 1994 to 1995 eruption, Barren Island Volcano: evidence of dynamic magma plumbing system in the Andaman subduction zone. Geosci Front 5:113–126

Reutter K, Scheuber E, Helmcke D (1991) Structural evidence of origin parallel strike-slip displacements in the North Chilean Precordillera. Geol Rundsch 80:135–153

Richards JP (2003) Tectono-magmatic precursors for porphyry Cu–Mo–Au deposit formation. Econ Geol 98:1515–1533

Richards JP (2009) Postsubduction porphyry Cu-Au and epithermal Au deposits: products of remelting of subduction-modified lithosphere. Geology 37:247–250

Richards JP (2011) High Sr/Y arc magmas and porphyry Cu ± Mo ± Au deposits: just add water. Econ Geol 106:1075–1081

Richards JP, Kerrich R (2007) Adakite-like rocks: their diverse origins and questionable role in metallogenesis. Econ Geol 102:537–576

Richards JP, Boyce A, Pringle M (2001) Geologic evolution of the Escondida Area, Northern Chile: a model for spatial and temporal localization of porphyry Cu mineralization. Econ Geol 96:271–305

Richards JP (2002) Discussion on "Giant versus small porphyry copper deposits of Cenozoic age in northern Chile: adakite versus normal calc-alkaline magmatism" by Oyarzum et al. (Miner Depos 36:794–798, 2001). Miner Depos 37:788–790

Rohrlach BD, Loucks RR (2005) Multi-million-year cyclic ramp-up of volatiles in a lower crustal magma reservoir trapped below the Tampakan copper-gold deposit by Mio-Pliocene crustal compression in the Southern Philippine, vol 2. In: Porter TM (ed), Super porphyry copper and gold deposits—a global perspective. PGC Publishing, pp 369–407

Rojas G (2015) Petrografía, geoquímica y geocronología del distrito Los Volcanes Conchi, Región de Antofagasta, Chile, Undergraduate thesis, Earth Science Department, Universidad de Concepción, p 139

Rooney TO, Franceschi P, Hall CM (2011) Water-saturated magmas in the Panama Canal region: a precursor to adakite-like magma generation? Contrib Mineral Petrol 161:373–388

Santana, CA (2010) Informe estudio geológico-estructural y su aplicación a la exploración de cuerpos mineralizados en el distrito El Abra: Internal report from El Abra Company (SCMEA), p 25

Schütte P, Chiaradia M, Beate B (2011) Petrogenetic evolution of arc magmatism associated with Late Oligocene to Late Miocene porphyry-related ore deposits in Ecuador. Econ Geol 105:1243–1270

Shannon JR, Walker BM, Carten RB, Geraghty EP (1982) Unidirectional solidification textures and their significance in determining relative ages of intrusions at the Henderson Mine, Colorado. Geology 10:293

Sheppard SMF, Taylor HP (1974) Hydrogen and oxygen isotope evidence for the origin of water in the Boulder Batholith and the Bute ore deposits, Montana. Econ Geol 69:926–946

Shinohara H, Hedenquist JW (1997) Constraints on magma degassing beneath the far southeast porphyry Cu–Au deposit, Philippines. J Petrol 38:1741–1752

Sillitoe RH (1972) A plate tectonic model for the origin of porphyry copper deposits. Econ Geol 67:184–197

Sillitoe RH, Perelló J (2005) Andean copper province: tectonomagmatic settings, deposit types, metallogeny, exploration, and discovery. Econ Geol 100th Anniversary vol: 845–890

Simon AC, Ripley EM (2011) The role of magmatic sulfur in the formation of ore deposits. In: Behrens H, Webster JD (eds) Sulfur in magmas and melts: its importance for natural and technical processes. Mineralogical Society of America and Geochemical Society, Rev Miner Geochem 73:513–578

Skewes MA, Stern CR (1994) Tectonic trigger for the formation of late Miocene Cu-rich breccia pipes in the Andes of central Chile. Geology 22:551–554

Skewes MA, Stern CR (1995) Genesis of the giant Late Miocene to Pliocene Cu deposits of Central Chile in the context of Andean magmatic and tectonic evolution. Int Geol Rev 37:893–909

Sun SS, McDonough WF (1989) Chemical and isotopic systematics of oceanic basalts; implications for mantle composition and processes. In: Saunders AD, Norry MJ (eds) Magmatism in the ocean basins. Geol Soc of London 42:313–345

Tomlinson AJ, Dilles JH, Maksaev V (2001) Application of apatite U-Th/He thermochronometry to the determination of the sense and amount of vertical fault displacement at the Chuquicamata porphyry copper deposit, Chile—a discussion. Econ Geol 96:1307–1309

Williams-Jones AE, Heinrich CA (2005) 100th anniversary special paper: vapor transport of metals and the formation of magmatic-hydrothermal ore deposits. Econ Geol 100:1287–1312